Solid Earth Discuss., 6, 2423–2494, 2014
www.solid-earth-discuss.net/6/2423/2014/
doi:10.5194/sed-6-2423-2014

Solid Earth
Discussions
Open Access

3-D-geomechanical-numerical model of the contemporary crustal stress state in the Alberta Basin

K. Reiter[1,2] and O. Heidbach[1]

[1]GFZ German Research Centre for Geosciences, Telegrafenberg, 14473 Potsdam, Germany
[2]University of Potsdam, Institute of Earth and Environmental Science, Karl-Liebknecht-Straße 24–25, 14476 Potsdam-Golm, Germany

Received: 31 July 2014 – Accepted: 31 July 2014 – Published: 20 August 2014

Correspondence to: K. Reiter (reiter@gfz-potsdam.de)

Published by Copernicus Publications on behalf of the European Geosciences Union.

Abstract

In the context of examining the potential usage of safe and sustainable geothermal energy in the Alberta Basin whether in deep sediments or crystalline rock, the understanding of the in-situ stress state is crucial. It is a key challenge to estimate the 3-D stress state at an arbitrary chosen point in the crust, based on sparsely distributed in-situ stress data.

To address this challenge, we present a large-scale 3-D geomechanical-numerical model (700 km ×1200 km ×80 km) from a large portion of the Alberta Basin, to provide a 3-D continuous quantification of the contemporary stress orientations and stress magnitudes. To calibrate the model, we use a large database of in-situ stress orientation (321 S_{Hmax}) as well as stress magnitude data (981 S_V, 1720 S_{hmin} and 2 (+11) S_{Hmax}) from the Alberta Basin. To find the *best-fit* model we vary the material properties and primarily the kinematic boundary conditions of the model. This study focusses in detail on the statistical calibration procedure, because of the large amount of available data, the diversity of data types, and the importance of the order of data tests.

The *best-fit* model provides the total 3-D stress tensor for nearly the whole Alberta Basin and allows estimation of stress orientation and stress magnitudes in advance of any well. First order implications for the well design and configuration of enhanced geothermal systems are revealed. Systematic deviations of the modelled stress from in-situ data are found for stress orientations in the Peace River- and the Bow Island Arch as well as for leak-off-test magnitudes.

1 Motivation

The estimation of the in-situ stress state in the upper crust in addition to the understanding of earthquake cycles and plate tectonics, is crucial for exploration and production of energy resources. These include geothermal energy, hydrocarbons, CO_2 sequestration (carbon capture storage – CCS) and geotechnical subsurface constructions such as mines, tunnels, interim storage sites for natural gas and nuclear waste deposits. Reliable estimates of orientation and magnitude of the crustal stress field are desired before drilling. This is important in terms of well stability (e.g. Bell and McLellan, 1995; Peska and Zoback, 1995), but also related to well configuration of several corresponding wells (e.g. Bell and McLellan, 1995), in the case of reservoir stimulation by hydraulic fracturing. This is important in geothermal reservoirs (Enhanced Geothermal Systems – EGS) (Legarth et al., 2005; Wessling et al., 2009) and issues of inadequate understanding of the spatial stress pattern (e.g. Brown, 2009; Duchane and Brown, 2002). This is also true for hydrocarbon reservoirs or the evaluation of nuclear waste repositories (e.g. Fuchs and Müller, 2001; Gunzburger and Magnenet, 2014; Heidbach et al., 2013).

The stress tensor and its components are not to be measured directly, but there are several stress indicators, which allow estimation of several components of the stress tensor (e.g. Ljunggren et al., 2003; Schmitt et al., 2012; Zang and Stephansson, 2010). The following components of the stress tensor are potentially available: the azimuth of the maximum (or minimum) horizontal stress (S_{Hmax}), the vertical stress magnitude (S_{V}) as well as the magnitudes of the maximum and minimum horizontal stress (S_{hmin} and S_{Hmax}). However, the reliable estimation of the S_{Hmax} magnitude remains difficult as only shallow in-situ stress estimations are available or numerous assumptions have to be made that impose high uncertainties. Furthermore, stress informations are sparse and extra- or interpolation of few data records to the area or depth of interest is necessary.

However, stress estimation via interpolation techniques becomes in particular questionable in the case of structural inhomogeneities like faults, detachments (Bell and McLellan, 1995; Röckel and Lempp, 2003; Roth and Fleckenstein, 2001; Yassir and Bell, 1994), or varying material properties (Roche et al., 2013; Warpinski, 1989). Furthermore, drilling down to a geothermal reservoir requires reaching greater depths, as available measurements are delivered in the context of hydrocarbon production. For example in Alberta, deeper parts of the basin or the upper basement are the target depths (e.g. Hofmann et al., 2014; Majorowicz and Grasby, 2010a, b; Weides et al., 2013, 2014). Therefore, estimation of the stress state, especially at greater depth, is a challenge prior drilling.

An alternative approach to estimate the 3-D stress state is geomechanical-numerical modelling. This method has the advantage to incorporate structural and material inhomogeneity's that impose local to regional changes of the stress field. There are several studies on tectonic plate scale stress orientation patterns in 2-D (e.g. Coblentz and Richardson, 1996; Dyksterhuis et al., 2005; Humphreys and Coblentz, 2007; Jarosinski et al., 2006), large scale (regional) models in 3-D (Buchmann and Connolly, 2007; Hergert and Heidbach, 2011; Parsons, 2006), as well as local (reservoir scale) 3-D models (e.g. Fischer and Henk, 2013; Heidbach et al., 2013; Henk, 2005; Orlic and Wassing, 2012; Van Wees et al., 2003). Modelling of the contemporary stress field mainly depends on the structural model, the material properties, the initial stress state and the applied kinematic boundary conditions. However, the reliability of such models depends strongly on the model calibration towards in-situ stress data. Usually there is little in-situ stress data available for model calibration in published studies (e.g. Buchmann and Connolly, 2007; Fischer and Henk, 2013; Heidbach et al., 2013; Hergert and Heidbach, 2011), which rule out any statistic validation.

The Alberta Basin is a study area with well understood structures and material properties, and a large collection of in-situ stress data. We use this information to build a 3-D-geomechanical-numerical model of the Alberta Basin and surroundings with an extent of 1200 km × 700 km down to a depth of 80 km. The goal is to get the full tensor of the contemporary undisturbed stress state, called stress model in the following. These are 981 S_V magnitude data, 321 S_{Hmax} azimuth data, 1720 S_{hmin} magnitudes, 2 measured (overcoring), and 11 calculated S_{Hmax} magnitudes within the model region. There is no other basin with a comparable range of available in-situ stress data (Bell and Grasby, 2012). The availability of very good stress data allows for the calibration of the stress model vs. a never reached diversity, and number of in-situ stress indicators.

SED
6, 2423–2494, 2014

K. Reiter and O. Heidbach

The model calibration will be done in three consecutive steps: (1) density of basin infill, using S_V magnitude data, (2) orientation of kinematic boundary conditions using S_{Hmax} azimuth data, and (3) magnitudes of kinematic boundary conditions (strain) using S_{hmin} and S_{Hmax} magnitude data. As linear elastic rheology is used for the model, the linear dependency between the two applied strain magnitudes (push and pull) along the outer edges of the model is calculated. This allows, via planar regressions the calculation of the optimal strain magnitudes, providing the *best-fit* model. The application of the model would be for exploitation of hydrocarbons and more for exploration and design of a geothermal plant in the Alberta Basin. Additionally it may be used in crystalline rocks, mainly in case of necessary hydraulic stimulation. Mistaken investments e.g. parts of the Fenton Hill project (Brown, 2009; Duchane and Brown, 2002) could potentially be avoided with a better previous understanding of the 3-D in-situ stress state.

2 Modelling concept

2.1 Model assumptions

The compilation of stress data in North America by Adams (1987, 1989); Adams and Bell (1991); Bell et al. (1994); Fordjor et al. (1983); Gough et al. (1983); Sbar and Sykes (1973); Zoback and Zoback (1980, 1981, 1989, 1991) and recently by Reiter et al. (2014) resolved, that the pattern of S_{Hmax} orientations is largely uniform over thousands of kilometres. An assumption was that the same forces driving plate tectonics are the major control on the stress field, which is confirmed in first order (e.g. Richardson, 1992; Zoback et al., 1989; Zoback, 1992).

The stress pattern is driven and altered by several stress sources; they are discriminated depending on the scales in first order- (> 500 km), second order- (100–500 km) and third order stress sources (< 100 km) (Heidbach et al., 2007, 2010; Müller et al., 1997; Tingay et al., 2005; Zoback, 1992; Zoback and Mooney, 2003). First order stress sources as the main driving forces are summarized as: plate boundary forces, which are ridge push, slab pull, and trench suction, gravity and basal drag by mantle convection. Second order stress sources are lithospheric flexure, localized lateral density, stiffness and strength contrasts, topography, large fault zones, and lateral contrasts of heat production. Third order stress sources are local density, stiffness or strength contrasts, basin geometry, basal detachment, incised valleys, and anthropogenic stress changes.

Under the parameters to reproduce the crustal stress field of the Alberta basin, the model has to be large enough to portray the first and second order stress sources. Whereas the first order stresses sources, which control plate tectonic motion, are represented by the kinematic boundary conditions, the second- and third order stress sources are represented by the model geometry. This is possible, when structures are known and convertible to the model. As inhomogeneous topography and mass distribution within the lithosphere have a major impact on the stress orientation (Camelbeeck et al., 2013; Ghosh et al., 2009; Humphreys and Coblentz, 2007; Naliboff et al., 2012), it is crucial to incorporate the major structural units in the crust and upper mantle in the model geometry.

Linear elastic material properties are an accurate approximation as long as the strain ($\boldsymbol{\epsilon}$) is small enough, and no failure occurs. This might be assumed for the Alberta Basin, which is seismically relatively quiescent. Documented earthquakes are usually restricted to the Rocky Mountains, foothills, and suspected man-made clustered events (e.g. Baranova et al., 1999; Schultz et al., 2014).

Our focus is the Alberta Basin and the uppermost basement below the basin due to our key interest in the investigation of the potential usability of deep geothermal energy (EGS). Furthermore, the calibrations data are from the sediments up to a depth of about 5 km with no deeper stress indicators are available. Exceptions to this are three S_{Hmax} azimuths, derived from focal mechanisms solutions.

Viscous rock deformation, acceleration, changing pore pressures as well as other thermal effects influences the stress state, but as we strive to model the contemporary

SED
6, 2423–2494, 2014

K. Reiter and O. Heidbach

undisturbed total stress tensor (stress model) these processes are assumed to have only marginal influence and are disregarded in the model. We assume that the following model assumptions are sufficient to estimate the contemporary 3-D stress state within the Alberta basin and upper basement:

- Large scale geometry of the model down to the upper mantle is crucial (main structural units only).
- Linear elastic material properties are used.
- Gravity as the body force.
- The lateral kinematic boundary conditions of the model are a parameterization of ongoing plate tectonic motion, effects of lateral density contrasts (gravitational potential energy) of outside of the model, and remnant stresses from terminated tectonic processes.

Due to the complex structures and inhomogeneous materials properties, an analytical solution cannot be estimated. Thus, we use for the discrete solution the finite element method (FEM), as it allows to use unstructured meshes, for a good representation of the 3-D model structure. With these assumptions the model is described with the partial differential equations of the equilibrium of forces:

$$\frac{\partial \boldsymbol{\sigma}_{ij}}{\partial x_j} + \rho x_i = 0, \tag{1}$$

where $\partial \boldsymbol{\sigma}_{ij}$ is the change of total stress, ∂x the change of length and ρx represents the weight of the rock section (ρ = density).

After model design (structural model) and definition of material properties (ρ, Young's Modulus, density), the partial differential equation (Eq. 1) can be calculated within given kinematic boundary conditions. The latter will be varied to find the *best-fit* model. This is the stress model together with material properties and kinematic boundary conditions, which deliver the best fit for all in-situ stress data.

SED
6, 2423–2494, 2014

2.2 General workflow of model calibration

Generally a model has to be calibrated before application or interpretation. The general concept, independent from the technical context, is to test the model's outcome vs. in-situ data. Such data are called model-independent data in contrast to model-dependent data, which are used to generate the model.

In this study the lithological and tectonic structures, the rheology, the body force, the initial stress state, and the kinematic boundary conditions are the model-dependent data (Fig. 1). Based on these data the structural model is defined, which is discretized to a (unstructured) mesh and assembled together with the material properties, body forces, the boundary conditions, and the initial stress state. Available in-situ stress data are the model-independent data. These are the S_V magnitudes, the S_Hmax azimuth data, and S_hmin and S_Hmax magnitudes. The modelled stress tensor is tested against the in-situ data. When one dataset is tested successfully, the next dataset is used in the next calibration step. Otherwise the material properties or boundary conditions are optimized as long as the test is successful.

First, the stress model is tested vs. in-situ S_V magnitudes, to conclude estimation of density (material properties and body force). In the second step the S_Hmax orientation is tested to determine the orientation of applied kinematic boundary conditions. In the final step, S_hmin and S_Hmax magnitudes are used to calibrate the applied magnitudes of the kinematic boundary conditions. When all model-independent datasets are tested successfully, the *best-fit* model is found and is a subject of further use (interpretation and application).

The model-depended data, construction and compilation process of the geomechanical model is described in Sect. 3, whereas the model independent data are introduced in Sect. 4. The calibration procedure is presented in detail in Sect. 5. Finally the discussion can be found in Sect. 6.

SED
6, 2423–2494, 2014

3 Model setup

3.1 Geometry of the Alberta Basin

3.1.1 Tectonic and sedimentary history of the Alberta Basin

The Alberta Basin (Fig. 2) occupies a large portion of the much larger Western Canada Sedimentary Basin (WCSB). Starting from north-east clockwise it is bounded by the Canadian Shield, the Bow Island Arch, the Rocky Mountains and the Tathlina High in the north. The crystalline basement of the WCSB and implicitly of the superposed Alberta Basin, is the North American craton exposed by erosion to the north-east as the Canadian Shield (Boerner et al., 2000; Flowers et al., 2012; Hoffman, 1989; Ross et al., 1994, 2000). The main structural units of the Alberta basement are the Buffalo Head Terrane (Aulbach et al., 2004), the Taltson Magmatic Zone (e.g. Chacko et al., 2000), the Hearne Province (Hajnal et al., 2005) and the Trans-Hudson Orogen (e.g. Corrigan et al., 2005; Németh et al., 2005) and other smaller units, which welded together between 1.8 and 2.0 Ga. There are two important lineaments, the Snowbird Tectonic Zone (STZ – Ross et al., 2000, and references therein) and the Great Slave Lake Shear Zone (GLS – Sami and James, 1993), and their continuation (Hay River fault zone).

Sediments were deposited in the basin, interrupted by a few discontinuities during the whole Phanerozoic (Mossop and Shetsen, 1994a, Chapter 6–26). Mainly shelf sediments deposited onto the craton as recently as the Upper Jurassic. At that time, sedimentation character changed, and the basin developed to a rapidly subsiding fore-deep trough (Poulton et al., 1994). Mature sediments were previous derived from north-east, and changed to less mature sediments, derived from the west. The change to terrestrial deposits in Early Cretaceous (Smith, 1994) coincides with first the Ominicean Orogeny, and later the Lamariden Orogeny (Porter et al., 1982; Price, 1981; Wright et al., 1994). Jurassic to Palaeocene strata mainly deposited in the western part of the Alberta Basin and have been incorporated in the Rocky Mountains fold-and-thrust belt (foothills and front ranges – Fig. 3). This is bound farther west (main ranges) in British Columbia by

SED
6, 2423–2494, 2014

the Rocky Mountain Trench. The final shape of the Alberta foreland basin developed by downward flexing of the Canadian Shield due to lithospheric loading and isostatic flexure in a retro-arc setting (Leckie and Smith, 1992; English and Johnston, 2004), together with the sediments derived from the developing Canadian Cordillera (Gabrielse and Yorath, 1989). The Alberta Basin consists of a nearly undeformed sedimentary wedge (Fig. 3), that increases in thickness from zero at the Canadian Shield to approximately 5500 m near the fold-and-thrust belt. The overall wedge shape in the Alberta Basin, perpendicular to the Rocky Mountains is quite homogeneous from north-west to south-east.

Only the Peace River Arch close to the Rocky Mountains is striking within the homogeneous wedge, which is indicated by several geophysical investigations. There are several explanations: elevated Precambrian basement (Bell and Babcock, 1986; Bell, 1996b; Bell and Grasby, 2012; Halchuk and Mereu, 1990), the occurrence of mafic sills, which intruded in the upper crust of the Peace River Arch (Eaton et al., 1999) and/or lateral heterogeneities (transfer zone or local rheological properties in Bell and McCallum, 1990), a softer inclusion (Dusseault and Yassir, 1994) or crustal thinning caused by extension Bouzidi et al. (2002).

3.1.2 Model geometry

The model box of Alberta, indicated in Fig. 4, is oriented parallel or perpendicular to the observed basin structure (Fig. 2), the orientation of S_{Hmax} (e.g. Bell et al., 1994; Reiter et al., 2014, see rose diagram in Fig. 4), the wedge shape of the Alberta Basin (Fig. 3), the thermally-defined Cordillera–Craton boundary (Hyndman et al., 2009) and the overall plate motion of the North American Craton, measured by GPS (Henton et al., 2006; Mazzotti et al., 2011).

The model has a south-west to north-east striking extent of 700 km, and 1200 km in north-west to south-east direction (Fig. 4), and 80 km in depth. For the definition of the model geometry it was necessary to choose the geometrically relevant structures, strength contrasts or density variations. These can potentially affect the stress field,

SED
6, 2423–2494, 2014

K. Reiter and O. Heidbach

while considering limitations of the possible number of finite elements. The main structural units are the mantle, the crustal basement, the sedimentary basin, the foothills, the Rocky Mountains and the Elk-Point evaporates, within the basin due to their potential to detach the stresses of the supra-salt units from the sub-salt units. Furthermore, the Snowbird tectonic zone and the Great Slave shear zone are incorporated and cut the basement and the sediments.

The deepest implemented boundary is the Mohorovičić-discontinuity (Moho) as the crust-mantle transition. We use various geophysical data to define the Moho topography by directional kriging (Fig. 5). These are data from seismic refraction studies (Bouzidi et al., 2002; Burianyk et al., 1997; Clowes et al., 2002; Fernández-Viejo and Clowes, 2003; Halchuk and Mereu, 1990; Németh et al., 1996, 2005; Spence and McLean, 1998; Welford et al., 2001; Zelt and White, 1995) and from teleseismic studies (Gu et al., 2011; Shragge et al., 2002).

The basement top (Fig. 6) is defined as the boundary between the basement (southwestern continuation of the Canadian Shield) and the sedimentary basin. It is constructed by discrete smoothing interpolation (DSI – Mallet, 1992), based on 7257 well data available from the Alberta Geological Survey (AGS).

The strata overlying the Precambrian basement are subdivided into the Rocky Mountains, the foreland fold-and-trust-belt (foothills) and the sediments within the basin (Fig. 7). The first set consists of allochthonous Palaeozoic strata, whereas the foothills consists of the same stack of sediments from the entire Phanerozoic, deposited in the Western Canadian Sedimentary Basin. For a definition of the boundary between these parts, geological maps and interpreted cross-sections were used (Mossop and Shetsen, 1994b; Price, 1994; Wright et al., 1994).

Salt deposits within the sedimentary column have the possibility to geomechanically detach the stresses in the upper rock units from the long wave-length stresses at depth (Bell, 1993; Roth and Fleckenstein, 2001; Röckel and Lempp, 2003; Tingay et al., 2005). The Devonian Elk Point Group contains several salt deposits (Grobe, 2000; Meijer Drees, 1994). These up to 380 m thick deposits (Figs. 3 and 7) have been rec-

SED
6, 2423–2494, 2014

ognized within five stratigraphic formations. They are ordered from oldest to youngest: Lower Lotsberg, Upper Lotsberg, Cold Lake, Prairie Evaporate and Hubbard Evaporate salts. The Elk Point evaporates are separated from the other basin sediments (Mossop and Shetsen, 1994a, Chapter 8–26) as an independent unit; evaporate strata with a thickness of ≥ 100 m are used based on data from Grobe (2000). All these interfaces are also generated with the DSI algorithm from Mallet (1992). Finally the model box is completed with the digital elevation model (DEM) from the USGS (2008).

3.1.3 Model discretization into finite elements

Our key goal is to model the contemporary 3-D stress state within the basin and in the upper part of the basement. To reproduce the thin rock salt layer within the basin, it was necessary to have a minimum element amount of six elements within the basin in z direction. This results in a vertical resolution of about 200 to 800 m for the upper model parts (Fig. 8). In x and y direction the resolution within the basin and the upper basement is about 5000 m. The element-thickness decreases with depth within the basement; down below to −25 km. In deeper parts (−25 to −80 km) the resolution is clearly coarser, about 20 km in all directions (Fig. 5). Thus, the whole model is build up from 349 690 hexahedrons, 4188 tetrahedrons, 552 pyramids and 474 prisms, which allow fast model runs.

3.2 Rock properties

To calculate the stresses, the Young's modulus (E) and the Poisson's ratio (v) are the essential geomechanical material properties. The body forces of the rock units are represented by the density (ρ). Mantle density below Alberta ranges between 3346 and 3366 kg m^{-3} according to White et al. (2005). For this model a density of 3350 kg m^{-3} for the mantle is used (Table 1). The density of the Canadian Shield ranges between 2640 and 2830 kg m^{-3} (White et al., 2005), with this model using a value of 2800 kg m^{-3}. Young's modulus and Poisson's ratio of the basement are calculated based on the V_p and V_s data from northern Alberta (Dalton et al., 2011). The dynamic Young's modulus and the Poisson's ratio (0.21–0.22) are calculated according to Mavko et al. (2009). Based on the dynamic Young's modulus, the static Young's modulus is calculated according to King (1983) and Wang et al. (2000) with a range of 1.02×10^{10} to 8.56×10^{10} Pa. In the model, 0.21 and 7.0×10^{10} are used as Poisson's ratio and Young's modulus respectively for the basement, which is in agreement to data from Turcotte and Schubert (2002). Most Phanerozoic sediments overlying the basement, including the foothills and the Rocky Mountains, are mainly clastic sediments (e.g. sandstone or shale) and limestone with the exception of the separated evaporates. These material properties are estimated based on Fossen (2010); Okrusch and Matthes (2005); Turcotte and Schubert (2002), see Table 1.

3.3 Initial stress state

Deformation of the model due to gravity driven subsidence is not desired. Therefore an initial stress state of the model is derived, which is in equilibrium with the body forces (gravity). For the initial stress state uniaxial strain conditions (Eq. 2) or lithostatic stress conditions for greater depth (Heim, 1878, Eq. 3) are often assumed.

$$S_{\mathrm{Hmean}} = \frac{S_{\mathrm{Hmax}} + S_{\mathrm{hmin}}}{2} = S_{\mathrm{V}} \left(\frac{\nu}{1-\nu} \right) \tag{2}$$

$$S_{\mathrm{Hmax}} = S_{\mathrm{hmin}} = S_{\mathrm{V}} \tag{3}$$

$$k = \frac{S_{\mathrm{Hmean}}}{S_{\mathrm{V}}} = \frac{S_{\mathrm{Hmax}} + S_{\mathrm{hmin}}}{2S_{\mathrm{V}}}. \tag{4}$$

Using uniaxial strain conditions ($k = 1/3$, when ν is 0.25, Eq. 2) or lithostatic conditions ($k = 1$, Eq. 3), the stress ratio k (Eq. 4) is constant for both, when plotting vs. depth. But when k is plotted vs. depth, based on in-situ data, the discrepancy is obvious (e.g. Brown and Hoek, 1978; Gay, 1975, Fig. 9a). Visible are increasing k values close to

SED
6, 2423–2494, 2014
Calibration of 3-D crustal stress model Alberta Basin
K. Reiter and O. Heidbach

the surface. Thus, assuming lithostatic or uniaxial conditions is apparently insufficient for appropriate initial stress conditions.

Sheorey (1994) provides a simple spherical earth model for tectonically calm regions with no significant lateral density- and strength contrasts. In this model k is a function (Eq. 5) of the Young's modulus (E in GPa) and depth (z in m). This was confirmed by later published in-situ stress magnitudes from the KTB borehole (Brudy et al., 1997, see Fig. 9a).

$$k = 0.25 + 7E\left(0.001 + \frac{1}{z}\right), \quad (5)$$

When the model is embedded in an extended model with inclined edges, it is possible to find a fit of the k values vs. depth from the model. This is in comparison to a synthetic depth distribution, based on the Sheorey-equation (Eq. 5). This technique is so far used only occasionally (Buchmann and Connolly, 2007; Hergert and Heidbach, 2011). By generating the initial stress model, settlement due to the gravitational load occurred. Using the initial stress condition in the stress model, settlement in the model (< 1 m) can be neglected in relation to the model size.

For comparison the calculated k ratio, Eq. (5) from Sheorey (1994), and the initial k ratio from the model of Alberta is plotted vs. depth. Material properties are adjusted for the initial model only, until good agreement is obtained. Exemplary two of them are plotted for illustration (Fig. 9b and c). From a purely technical point of view, the initial stress conditions were determined after calibration of the used sediment density.

3.4 Boundary conditions

Henton et al. (2006) and Mazzotti et al. (2011) showed that surface strain measured by GPS indicates strain rates are below the measurement error within Alberta and the Rocky Mountains. More to the west in the Intramontane Belt the values are also very low. Yet in the coastal cordilleras, rates of about 10–15 mm yr^{-1} in north-east direction

SED
6, 2423–2494, 2014

with respect to stable North America are observed. The North American Eulerian rotation pole is located south-west of Ecuador, resulting in a counter-clockwise rotation of about 20 mm yr^{-1} in south-west direction in Alberta (Henton et al., 2006). Flesch et al. (2007) found, that (deviatoric) stresses associated with the accommodation of relative plate motion are in the same order of magnitude as buoyancy forces (gravitational potential energy – GPE). The orientation of observed North American rotation, shortening in the Canadian Cordillera (Henton et al., 2006; Mazzotti et al., 2011), and of GPE gradient orientation (Flesch et al., 2007) corresponds to the observed average S_{Hmax} azimuths in Alberta (see rose diagram in Fig. 4).

As the model edges are parallel and perpendicular, respectively to the observed plate motion, PGE and horizontal stress azimuth, displacement at the model boundaries will be applied orthogonal to the side walls of the model box. Horizontal and vertical motion is allowed along the side walls (Fig. 4). The applied amount and orientation of push (towards north-east) and pull (towards south-east) along the model will be tested during the calibration phase of the model. The bottom of the model is fixed in z direction, lateral motion within the extend of the model box is allowed.

4 In-situ stress data

This section presents a short introduction into the terminology used for the stress data during the model calibration procedure.

4.1 Orientation and magnitudes of stresses in sedimentary basins

The 3-D stress in rock ($\boldsymbol{\sigma}$) is described with a second-order tensor. By choosing an principal coordinate system, the stress tensor ($\boldsymbol{\sigma_{ij}}$)

$$\boldsymbol{\sigma_{ij}} = \begin{pmatrix} \sigma_{11} & \sigma_{12} & \sigma_{13} \\ \sigma_{21} & \sigma_{22} & \sigma_{23} \\ \sigma_{31} & \sigma_{32} & \sigma_{33} \end{pmatrix} \text{ or } \begin{pmatrix} \sigma_{xx} & \sigma_{xy} & \sigma_{xz} \\ \sigma_{yx} & \sigma_{yy} & \sigma_{yz} \\ \sigma_{zx} & \sigma_{zy} & \sigma_{zz} \end{pmatrix}, \tag{6}$$

can be expressed with the three principal stresses:

$$\hat{\boldsymbol{\sigma}}_{ij} = \begin{pmatrix} \sigma_1 & 0 & 0 \\ 0 & \sigma_2 & 0 \\ 0 & 0 & \sigma_3 \end{pmatrix}. \tag{7}$$

These act normal to the principal planes and are the following: $\sigma_1 > \sigma_2 > \sigma_3$, in the order of magnitude. As the earth surface is a free surface and sedimentary basins are roughly flat at the top, it is often assumed that the vertical stress (S_V) is a principal stress. With this assumption the minimum horizontal stress (S_{hmin}) and the maximum horizontal stress (S_{Hmax}) (e.g. Jaeger et al., 2009; McGarr and Gay, 1978; Schmitt et al., 2012) are also principal stresses that are orthogonal to each other (Fig. 10). Their relative magnitudes determine the stress regime (Anderson, 1951, cited in Kanamori and Brodsky, 2004):

- Normal Faulting: $S_V > S_{Hmax} > S_{hmin}$
- Strike Slip: $S_{Hmax} > S_V > S_{hmin}$
- Reverse Faulting: $S_{Hmax} > S_{hmin} > S_V$.

More detail can be found in Amadei and Stephansson (1997); Jaeger et al. (2009); Schmitt et al. (2012); Zang and Stephansson (2010); Zoback (2007).

4.2 Contemporary stress field in the Alberta Basin

The present day stress field in Alberta has been a subject of several studies. It started with Bell and Gough (1979) recognizing in the Alberta Basin that borehole breakouts are an indicator of crustal stresses orientation (Fig. 10). They found that the S_{Hmax} azimuth is uniform oriented south-west to north-east in substantial parts of the Alberta Basin (Fig. 11). This observed orientation is perpendicular to the Rocky Mountain trench, which was confirmed by Adams and Bell (1991); Bell and Gough (1981);

SED
6, 2423–2494, 2014

Bell et al. (1994); Fordjor et al. (1983) and recently by Reiter et al. (2014). Orientation data are derived from a large variety of rock types, depths, and from different indicators. These are borehole breakouts at a depth range of 113–5485 m (Bell et al., 1994), geological indicators (Bell, 1985), drilling induced tensile fractures (Fordjor et al., 1983) and seismological studies in the Canadian Cordillera (Ristau et al., 2007), confirmed the overall orientation pattern (Fordjor et al., 1983). Only a counter-clockwise rotation of about 10–20° is observed in northern Alberta over the Peace River Arch.

The same homogeneous stress orientation is observed over wide areas of the North American plate (Bell and Gough, 1979; Adams and Bell, 1991; Fordjor et al., 1983; Gough et al., 1983; Reiter et al., 2014; Sbar and Sykes, 1973; Zoback and Zoback, 1980), which indicates that south-west to north-east stress orientation is present over the whole lithosphere rather than sediments only (Fordjor et al., 1983). This implies also that the sediments are attached to the basement (Bell, 1996b). The S_{Hmax} orientation is at a right angle to the Rocky Mountains fold axis. Therefore, the stress field responsible for thrust faulting in Mesozoic time is still present (Bell and Gough, 1979). The driving force of the observed stress pattern is plate tectonics, either by drag resistance of the lithosphere sliding over asthenosphere (Bell and McLellan, 1995; Zoback and Zoback, 1980) or mantle convection propelling the lithosphere (Bell and Gough, 1979; Fordjor et al., 1983; Gough, 1984).

The depth gradient of S_{V} and S_{hmin} increase from basin centre towards the foothills and the Rocky Mountains (Baranova et al., 1999; Bell, 1996b; Bell and Bachu, 2004; Bell and Grasby, 2012). This trend coincides with higher organic maturity (England and Bustin, 1986; Nurkowski, 1984) and larger compaction (Bell and Bachu, 2004) in that direction, which is related to depth of present and past burial. The maximum erosion of basin sediments is by about 1400 m (Woodland and Bell, 1989), uplift occurring since mid-Cenozoic time mainly is in the foothills (Bell and McLellan, 1995).

The stress regime in the basin sediments changes from thrust faulting in the foothills to strike slip within the basin, up to normal faulting regime further east in Saskatchewan (Bell and Gough, 1979; Bell et al., 1994; Bell and McLellan, 1995; Bell and Bachu,

SED
6, 2423–2494, 2014

K. Reiter and O. Heidbach

2003; Bell and Grasby, 2012; Woodland and Bell, 1989). A similar change from surface to depth is observed: from thrust faulting in < 350–600 m depth, strike slip in a depth range of about 500–2500 m, down to normal faulting in greater depths > 2500 m (Bell and Babcock, 1986; Fordjor et al., 1983; Jenkins and Kirkpatrick, 1979). There is also a varying S_{hmin} gradient discussed (Bachu et al., 2008; Bell and Grasby, 2012; Hawkes et al., 2005), but this is may be due to different measurement methods (Bell et al., 1994) or man-made stress changes. The $S_{\mathrm{Hmax}}/S_{\mathrm{hmin}}$ ratio in the Alberta Basin is about 1.3–1.6 (Fordjor et al., 1983).

Man-made stress perturbation due to hydrocarbon production or acid gas injections (e.g. Bachu et al., 2008; Bell and Grasby, 2012; Woodland and Bell, 1989) reduces or increases reservoir fluid pressure respectively, but has likely only local effects (e.g. Altmann et al., 2010). Furthermore, Baranova et al. (1999) found a strong correlation between rates of gas production and the number of seismic events, which is reasonable because production lead to decrease of S_{V} and increase of S_{Hmax} – consequentially increasing differential stresses. The stress change due to the gas extraction point to a regime which favours thrust faulting (Baranova et al., 1999). Hydraulic fractures applied for hydrocarbon industry or for enhanced geothermal systems deeper than 350 m will open parallel to south-west to north-east oriented S_{Hmax} orientations except in the Peace River Arch, they will tend to south-soutwest to north-northeast (Bell et al., 1994; Bell and Grasby, 2012). Close to the Rocky Mountains foothills, north-west to south-east oriented hydraulic fractures are possible, parallel to the thrust planes and the fold axes (Bell and Babcock, 1986). However, horizontal wells e.g. for EGS should be designed parallel to the S_{hmin} orientation (Bell and Grasby, 2012).

SED
6, 2423–2494, 2014

4.3 In-situ stress data

4.3.1 Vertical stress (S_V)

The vertical stress (S_V) is the overburden load, which is estimated using density logs (e.g. Gardner and Dumanoir, 1980) in a well:

$$S_V = \int_0^z \rho(z) g \, \mathrm{d}z \approx \overline{\rho} g z. \quad (8)$$

For the Alberta model region 981 S_V magnitude data sets are available (provided by the AGS), these are indicated by black points in Fig. 12. S_V magnitude data vary only slightly, even in greater depths, the lateral variation is less than 5 MPa.

4.3.2 Orientation of maximum horizontal stress (S_{Hmax})

The orientation of S_{Hmax} are indicated by borehole breakouts, focal mechanisms, hydraulic fracturing, overcoring, drilling induced fractured and geological indicators (for overview see: Bell, 1996a; Ljunggren et al., 2003; Schmitt et al., 2012; Zang and Stephansson, 2010; Zoback et al., 2003). 321 S_{Hmax} azimuth data sets are available for the modelled region in Alberta; these are indicated in Fig. 11, based on the latest update of the Canadian stress database (Reiter et al., 2014).

4.3.3 Magnitude of minimum horizontal stress (S_{hmin})

The S_{hmin} magnitudes are measured by hydraulic fracturing or the similar leak-off test. During hydraulic fracturing (Bell, 1996a; Haimson and Cornet, 2003; Hubbert and Willis, 1957; Zoback et al., 2003) and leak-off tests (e.g. Li et al., 2009; White et al., 2002; Zhou, 1997), the down-hole pressure is increased up to pressure loss due to fluid leakage in the rock mass. This happens, when the hydraulic fracture splits apart

SED
6, 2423–2494, 2014

the surrounding rock perpendicular to the least principal stress (σ_3), usually assumed to be S_{hmin} in sedimentary basins, and therefore the fracture opens in S_{Hmax} orientation (Fig. 10). The highest pressure is the fracture breakdown pressure (FBP, Haimson and Fairhurst, 1969), which is S_{hmin} + rock resistance up to failure. When the pressure at which the fracture closes or re-opens is less than S_{V}, it is assumed that S_{hmin} is measured (Haimson and Fairhurst, 1969). The mini-frac test (e.g. McLellan, 1987; Woodland and Bell, 1989) and the micro-frac test (Gronseth and Kry, 1983) as hydrofracturing methods estimate the closure pressure by opening and closing the fracture several times, but differs by the injected fluid volume.

The term "leak-off tests" is variably used and can be distinguished by their aim into formation integrity tests (FIT), "classic" leak-off tests (LOT) and extended leak-off tests (XLOT) (White et al., 2002). The general method is similar, but differs in pumping cycles and the point at which the pumping is stopped. Usually Leak-off tests (LOT) are meant, which provide the upper limit of S_{hmin} and measure the fracture closure pressure (FCP) or the instantaneous shut-in pressure (ISIP) (White et al., 2002). Extended leak-off tests (XLOT) allow measuring the fracture re-opening pressure, like originally hydrofracture tests.

For the model region, 1720 S_{hmin} magnitudes data are available, provided by the AGS; see Fig. 12. These are 784 leak-off magnitude data and 936 magnitude data from hydraulic fracturing. The different hydraulic fracturing methods are 14 Micro-frac, 91 Mini-frac, 250 Hydro-Frac-AIP, and 581 Hydro-Frac-FBP data. The data scatter strongly, independently from the test method or lithology. Further detailed information about the measurements are not available; that would allow whether the data represents the undisturbed stress state or not. The scatter either reflects the spatial anisotropy of the in-situ stress or that the data set is noisy, i.e. a mix of in-situ stress information and data from areas with a disturbed stress field.

SED
6, 2423–2494, 2014

K. Reiter and
O. Heidbach

4.3.4 Magnitude of maximum horizontal stress (S_{Hmax})

The magnitude of S_{Hmax} is measured via overcoring method (McGarr and Gay, 1978; Obert, 1962), which isolates a rock cylinder from the surrounding rock and measures the elastic relaxation of the rock cylinder. This is equivalent to the stress magnitude as well as the stress orientation, before removal of the surrounding rock. The drawbacks are the small quantity of inspected rock mass and that the application is usually close to the surface. Furthermore, there are several methods used to calculate S_{Hmax}, based on S_{hmin} magnitudes and known rock properties (e.g. Schmitt et al., 2012). For the model region, 11 calculated data (Bell et al., 1994) and 2 shallow measured data (overcoring from Kaiser et al., 1982) are available (see Fig. 12).

5 Model calibrations

5.1 General comparison technique

The 3-D geomechanical-numerical model (with the initial stress state) from Alberta will be calibrated in the following according to the work flow scheme (Fig. 1). Each type of in-situ stress data will be used step by step to calibrate the model. We first use the S_V data to calibrate the density (technical the initial stress state is found after this step), then we use the S_{Hmax} azimuth data to calibrate the orientation of applied kinematic boundary conditions. Finally the S_{hmin} and S_{Hmax} magnitudes are used to calibrate the magnitude of applied kinematic boundary conditions, i.e. push and pull at the edges of the model box.

In each step, the modelled stress tensor is interpolated via inverse distance interpolation onto each point, where in-situ stress data are available. The difference (ΔS) between measured stress ($S_{measured}$) and the modelled stress (S_{model}) is always calculated in the following way:

$$\Delta S = S_{measured} - S_{model}, \tag{9}$$

SED
6, 2423–2494, 2014

K. Reiter and O. Heidbach

which means, that negative values indicates an overestimation by the model and vice versa. A value close to zero indicates a good approximation of the in-situ stresses by the model. To compare magnitude data independently from the range, the deviation is normalized by the modelled stress value:

$$n\Delta S = \frac{S_{\text{measured}} - S_{\text{model}}}{S_{\text{model}}}. \tag{10}$$

To evaluate the differences between each in-situ data set and the model as a whole, the median of ΔS ($\widetilde{\Delta S}$) is calculated as a single value for each model. In the case of the *best-fit* model, the $\widetilde{\Delta S}$ shall be close to zero. To estimate the influence of outliers and the variation of the data, the mean ($\overline{\Delta S}$) and the standard deviation (SD) are also calculated. The linear correlation between the in-situ data and the model data is represented by the Pearson product-moment correlation coefficient (r), where $r = 1$ indicates total positive correlation, $r = -1$ total negative correlation and $r = 0$ no correlation.

The data-sets are contaminated with unlikely in-situ data; such data are often sorted out (e.g. Bell and Bachu, 2004; Bell and Grasby, 2012) for interpolation. As statistical tests are used in this study, data weed out is not required.

5.2 Calibration of material density on S_V data

The density of the sedimentary basin is calibrated based on S_V magnitudes ($n = 981$, Fig. 12); all other material properties are defined in Sect. 3.2. An overall density of the modelled basin sediments is tested with 2200, 2300 and 2400 $\text{kg}\,\text{m}^{-3}$. According to Eq. (9), the difference between the measured and modelled S_V (ΔS_V) as well the normalized ΔS_V ($n\Delta S_V$) is calculated:

$$\Delta S_V = S_{V\ \text{measured}} - S_{V\ \text{model}}. \tag{11}$$

$$n\Delta S_V = \frac{S_{V\ \text{measured}} - S_{V\ \text{model}}}{S_{V\ \text{model}}}. \tag{12}$$

SED
6, 2423–2494, 2014

The model with a density of 2200 kg m^{-3} has a $\widetilde{\Delta S}_V$, which is close to zero (−0.09 MPa) and a $\overline{\Delta S}_V$ of 0.28 MPa, which is also close to zero (Fig. 13). A standard deviation of 5.58 MPa as well the Gaussian distribution in the normalized histogram (Fig. 14a) indicates, that there is no large data drift. The correlation coefficient of $r = 0.935$ indicates a good fit.

5.3 Calibration of the orientation of kinematic boundary conditions based on S_{Hmax} azimuth data

The S_{Hmax} orientation is to large extent contributed by the choice of the model boundary conditions. Within the model region, 321 S_{Hmax} orientation data are available. They are displayed together with the data aside of the model in the stress map from Alberta (Fig. 11). The observed stress pattern is quite homogeneous.

The applied kinematic boundary conditions act orthogonal to the model margins, in a horizontal direction. Whereas shortening is applied in north-east direction to the model, extension is applied in south-east direction (Fig. 4). According Eq. (9) the difference between the measured and modelled S_{Hmax} azimuth is calculated:

$$\Delta S_{\mathrm{Hmax\,Azi}} = S_{\mathrm{Hmax\,Azi\,Measured}} - S_{\mathrm{Hmax\,Azi\,Model}}. \tag{13}$$

The histogram of the ΔS_{Hmax} azimuths (Fig. 14b) displays a main cluster around zero with a $\widetilde{\Delta S}_{Hmax}$ azimuth of −0.81°. The main cluster ranges between −40° to 40°; a second (smaller) cluster ranges between 70° and 130° with a slight peak around 90°, which is exactly orthogonal to the main cluster. This second cluster at around 90° explains the large contrast between the median ($\widetilde{\Delta S}_{Hmax} = -0.81°$) and the mean ($\overline{\Delta S}_{Hmax} = 6.04°$) as well as the large SD of 31.71°. The *best-fit* orientation is found for a large range of push and pull magnitudes. Therefore, different oriented boundary conditions are not further tested.

SED
6, 2423–2494, 2014

K. Reiter and O. Heidbach

5.4 Calibration of the magnitude of kinematic boundary conditions by S_{hmin} and S_{Hmax} magnitude data

The S_{hmin} ($n = 1720$) and S_{Hmax} ($n = 13:2$ measured and 11 calculated) magnitude data (Fig. 12) are used to calibrate the magnitude of applied push and pull along the model edges (Fig. 4). The aim is a model, which mimics the S_{hmin} and S_{Hmax} in-situ magnitude data quite well. Several scenarios with different amount of push and pull are calculated, to estimate the range of push and pull, close to the *best-fit* model. In the following we focus in only four scenarios with a different amount of push and pull (Table 2). According to Eqs. (9) and (10) the difference between the measured and modelled S_{hmin} and S_{Hmax} magnitudes are calculated as well as the normalized difference.

$$\Delta S_{\text{hmin}} = S_{\text{hmin Measured}} - S_{\text{hmin Model}}, \tag{14}$$

$$\Delta S_{\text{Hmax}} = S_{\text{Hmax Measured}} - S_{\text{Hmax Model}}, \tag{15}$$

$$n\Delta S_{\text{hmin}} = \frac{S_{\text{hmin Measured}} - S_{\text{hmin Model}}}{S_{\text{hmin Model}}}, \tag{16}$$

$$n\Delta S_{\text{Hmax}} = \frac{S_{\text{Hmax Measured}} - S_{\text{Hmax Model}}}{S_{\text{Hmax Model}}}. \tag{17}$$

The calculated $\widetilde{\Delta S}_{\text{hmin}}$ and $\widetilde{\Delta S}_{\text{Hmax}}$ of four model runs (Table 2) are plotted in the push vs. pull diagram (Fig. 15a and b). To highlight the linear dependency between push and pull in an elastic model, colour coded isolines are plotted. Each model along the light blue line (Fig. 15a) would derive a model, which fits well to the in-situ S_{hmin} data. The same stands for the light blue line in Figs. 15b and S_{Hmax} data. As the determination of the *best-fit* model is intended, the intersection of both light blue lines from Fig. 15a and b would derive such a model. This is done with a bivariate linear regression based on the spatial distribution of the $\widetilde{\Delta S}_{\text{hmin}}$ and $\widetilde{\Delta S}_{\text{Hmax}}$ (Fig. 15c). This method provides the following equations, which describes the zero isoline (light blue line) as a linear function. These are for median $\Delta S_{\mathrm{hmin}} = 0$:

$$y = -0.2709 \cdot x - 171.1586, \tag{18}$$

and for the $\widetilde{\Delta S}_{\mathrm{Hmax}}$ zero isoline:

$$y = -10.6642 \cdot x + 725.1380. \tag{19}$$

By equalizing Eqs. (18) and (19):

$$x = \frac{725.1380 + 171.1586}{10.6642 - 0.2709}, \tag{20}$$

the *best-fit* model has a push from south-west of 86.24 m and a pull in south-east direction of 194.52 m (Table 2, last line).

The median values ($\widetilde{\Delta S}_{\mathrm{hmin}} = -0.005$ and $\widetilde{\Delta S}_{\mathrm{Hmax}} = 0.018$) fits quite well, the similar stands for the mean values ($\overline{\Delta S}_{\mathrm{hmin}} = 0.03$ and $\overline{\Delta S}_{\mathrm{Hmax}} = -2.76$). The distribution of the normalized S_{hmin} (Fig. 14c) displays a positive screwed distribution. The correlation coefficient of the in-situ S_{hmin} magnitude data and the modelled S_{hmin} is $r = 0.835$. The normalized *best-fit* of S_{Hmax} (Fig. 14d) displays two outlier; these are the only two measured S_{Hmax} magnitudes, measured in a depth of 152 m.

6 Discussions

6.1 Workflow and calibration

The general workflow of model calibration (Fig. 1) is similar to other studies on numerical stress field modelling (e.g. Buchmann and Connolly, 2007; Fischer and Henk, 2013; Heidbach et al., 2013; Hergert and Heidbach, 2011). However, in contrast to former studies, the amount in-situ stress data from the Alberta Basin allows a statistical comparison to the model results.

SED
6, 2423–2494, 2014

6.1.1 S_V calibration

Given to the large model size (1200 km × 700 km × 80 km), the Alberta Basin infill is considered as one material type only except the Elk-Point evaporates. The available dataset of 981 S_V magnitude data points (Fig. 12) could be used via linear regression, to calculate the overall density of the sedimentary basin. But, to incorporate the (minor) lateral effects of topography, the overall density is determined in the calibration process. Plotting the distribution of the normalized deviation ($n\Delta S_V$) in histogram Fig. 14a demonstrates a Gaussian distribution, which implies there is no process affecting data drift. As data spreading does not depend on the vertical depth, a slightly higher lithological resolution with linear increasing density into depth would most likely not deliver a much better data fit. This could be solved by incorporation of all stratigraphic units, which would go far beyond the goals of this study. The spatial plot of ΔS_V (Fig. 16) shows that in-situ S_V magnitudes are slightly higher close to the foothills. This is expected from former studies, showing S_V increases in south-west direction (e.g. Bell and Bachu, 2004; Bell and Grasby, 2012).

6.1.2 Calibration of S_{Hmax} orientation

The 321 data records of the S_{Hmax} azimuth (Fig. 11) are used to test the orientation of the applied kinematic boundary conditions. As long as a certain push in north-east and pull in south-east direction is applied orthogonal to the model box (Fig. 4), a good fit of the stress orientation (Fig. 14b and 17) is achieved. There was no variation of the boundary conditions (orientation of push and pull) necessary; due to the appropriate chosen model orientation.

The histogram of the ΔS_{Hmax} azimuth (Fig. 14b) displays two data clusters. The larger cluster displays a normal distribution around zero, which is confirmed by a $\widetilde{\Delta S}_{Hmax}$ azimuth of $-0.81°$. A second data cluster is distributed around 90°, which explains the high SD of 31.71°. This confirms the use the median instead of the mean (6.04°) to qualify the data fit. The second cluster with a deviation of around 90° is the orientation of S_{hmin} indicating that some of the used in-situ S_{Hmax} azimuth data, are likely miss-interpreted S_{hmin} orientations. Such incorrect interpretations are sometimes observed in borehole breakout data (Brudy and Kjørholt, 2001; Barton and Moos, 2010); in such cases drilling induced tensile fractures, originated during drilling, are misinterpreted as borehole breakouts. Other reasons for orientation of data with right angles to the major population (S_{hmin}) are mud cake padding along caved zones and the collapse of pre-existing open fractures, again parallel to S_{Hmax} (Bell and Babcock, 1986; Bell and Grasby, 2012). Therefore, this second (smaller) cluster around 90° rather confirms then disproves the good data fit by the model.

The alternative explanation would be a horizontal stress state close to isotropic. This would allow large stress rotation due to small local stress sources (Heidbach et al., 2007). However, from the provided data this explanation can ruled out and the previous stated explanation is much more likely.

There are two areas in the modelled region, where a systematic difference of the S_{Hmax} azimuth between the in-situ data and the model is visible (Fig. 17). These are the western Peace River arch (56° N, 118° W) and the Sweetgrass arch in the very south, close to the southern Bow Island Arch (50° N, 114° W). In the Peace River arch, in-situ S_{Hmax} is rotated by about 20–30° (Bell et al., 1994; Bell and Grasby, 2012). The causes of this rotation, (see discussion in Bell and Babcock, 1986; Bell and McCallum, 1990; Bell, 1996b; Bell and Grasby, 2012; Bouzidi et al., 2002; Dusseault and Yassir, 1994; Eaton et al., 1999; Halchuk and Mereu, 1990), are not well represented by the model.

Bell and Gough (1979) suggested that the S_{Hmax} orientation is orthogonal to the topography of the Rocky Mountains, but comparison close to the topography in the very south of Alberta displays a good fit between the in-situ data and the model. They appear more influenced by the overall orientation than by the topography, which is also found by Reiter et al. (2014).

In contrast, the clockwise rotation of about 25° with respect to the regional trend is obvious close to the Bow Island arch. Likely this systematic rotation is caused by

SED
6, 2423–2494, 2014

structural features along the Bow Island arch which are not incorporated in the model, then by the Rocky Mountain topography.

The Bow Island arch separates the Alberta Basin and the Walliston Basin. It is a north-eastward plunging Precambrian basement feature, which was activated during the Laramiden orogeny and may be associated with intrusions, similar to Eocene intrusions, about 200 km to the south in Montana (Podruski, 1988). The systematic S_{Hmax} rotation in that region is most likely affected by these basement features along the Bow Island arch.

6.1.3 S_{hmin} calibration

The largest amount of stress data are the S_{hmin} magnitudes ($n = 1720$, Fig. 12). These, with a few S_{Hmax} magnitudes ($n = 13-2$ measure and 11 calculated, Fig. 12), are used to find the *best-fit* magnitudes of the utilized boundary conditions.

A large number of models were tested, but only four of these are shown here (Table 2 and Fig. 15a and b). Based on this four test scenarios with different strain magnitudes, the *best-fit* model is determined via bivariate regression. Calculated is the intersection of zero-isolines of $\widetilde{\Delta S}_{\mathrm{Hmax}}$ and $\widetilde{\Delta S}_{\mathrm{Hmin}}$ (Fig. 15c) based on a plot of push vs. pull (Table 2, Fig. 15a and b). This is possible as linear elastic rheology is used in the model.

An evaluation as to whether the measured S_{hmin} magnitudes really represent S_{hmin} or only σ_3, because hydraulic fracturing tests provide the information on the smallest principal stress. The correlation between the in-situ S_{hmin} magnitudes vs. modelled σ_3 ($r = 0.837$) is negligible higher then vs. modelled S_{hmin} ($r = 0.835$). This indicates that in-situ S_{hmin} measurements in the Alberta Basin likely represent the magnitude of S_{hmin} and confirms the assumptions for sedimentary basins, being that S_{hmin} is the smallest principal stress (e.g. Jaeger et al., 2009; McGarr and Gay, 1978; Schmitt et al., 2012).

The spatial distribution of the ΔS_{hmin} (Fig. 18) indicates that larger differences between the in-situ and the modelled magnitudes mainly occur in region with clustered data. Slightly higher in-situ magnitudes are observed in the region 56° N, 121° W, in contrast to the slightly lower in-situ S_{hmin} magnitudes in region 55° N, 119° W.

The $n\Delta S_{\mathrm{hmin}}$ histogram in Fig. 14c displays a positive screwed distribution. This indicates that the model underestimates a larger portion of the S_{hmin} magnitudes, in contrast to the in-situ data.

To examine deviation reasons, Fig. 19 plots $n\Delta S_{\mathrm{hmin}}$ depending on depth with the measuring method is indicated. In-situ S_{hmin} LOT data provide rather positive $n\Delta S_{\mathrm{hmin}}$ values in shallow depths (< 500 m) and negative values in depth > 500 m relative to the modelled S_{hmin} magnitudes. This implies that the model derives smaller magnitudes compared to shallow LOT magnitudes and larger ones with respect to deeper LOT magnitudes. In contrast hydraulic fracturing data did not indicate systematic deviations.

6.1.4 Deviation of Leak-off test (LOT) data vs. stress model

There are several reasons for the discrepancy of S_{hmin} in-situ LOT data vs. stress model, they are:

- Thrust faulting regime ($S_{\mathrm{hmin}} > \sigma_3$)
- Systematic measurement errors
- Systematic model errors
- Disturbed in-situ measurements

Thrust faulting regime ($S_{\mathrm{hmin}} > \sigma_3$)

Hydraulic fracturing (HF) and Leak-off tests (LOT) measure the smallest principal stress (σ_3), which is expected as S_{hmin} in sedimentary basins with normal faulting or strike slip stress regime. In a thrust faulting stress regime, in-situ data would underestimate S_{hmin}, as S_{V} is measured. However, the thrust faulting stress regime is expected in the Rocky Mountains, as well as in and close by the foothills (Bell and Gough, 1979;

Bell et al., 1994; Bell and McLellan, 1995; Bell and Bachu, 2003; Bell and Grasby, 2012; Woodland and Bell, 1989) and in shallow depths (up to 600 m) (Bell and Babcock, 1986; Fordjor et al., 1983; Jenkins and Kirkpatrick, 1979). Measuring $S_V = \sigma_3$ in shallow depth (< 500 m) instead of S_{hmin} would indicate a thrust faulting regime for some regions. But shallow LOT magnitudes are systematically larger than expected by the stress model, which excludes this attempt at explanation.

Systematic measurement errors

Alternatively, an overestimation of S_{hmin} by LOT could be explained, when the Formation Breakdown Pressure (FBP) or Leak-Off Pressure (LOP) (White et al., 2002) is measured. Additionally, LOT performed in shallow depth (< 300 m) are less reliable, because tensile strength of the rock plays a more significant role for the measured pressure (Bachu et al., 2008). These reasons would explain larger S_{hmin} magnitudes from LOT, compared to the model in shallow depth (< 500 m).

LOT are also used as Formation Integrity Tests (FIT) to determine whether the wellbore can sustain the stresses expected during drilling and production, then determine stress magnitudes (e.g. White et al., 2002). Such FIT data derives smaller magnitudes then the formation S_{hmin} magnitude. Furthermore, poor cement seal between the wellbore and the casing close to the LOT can reduce measured magnitude (Edwards et al., 1998). Both reasons could explain smaller S_{hmin} measurements in greater depth (> 500 m), derived from LOT magnitudes.

Systematic model errors

In-situ stresses are affected by the lithology at the locality (Roche et al., 2013; Warpinski, 1989). This is observed in the Alberta Basin where sandstone exhibits lower in-situ S_{hmin} magnitudes than shale (Bell and Grasby, 2012; Kry and Gronseth, 1983). As the modelled basin has only one material property, likely the Evaporate layer, the modelled stresses represents stress conditions from rocks, where in-situ stress data are derived. These are mainly sandstone and limestone, whereas leak-off-tests are usually conducted in shale (Bell and Grasby, 2012). Therefore, the drift could be explained by shallow shale and deeper sandstones or lime stone. Furthermore, extrapolation drift close to a free surface of a FEM model are sometimes observed.

Disturbed in-situ measurements

Man-made stress changes perturb the juvenile in-situ stress due to production (Bell and Grasby, 2012) and injection of fluids (Bachu et al., 2008), besides other mining activity. This is obvious, where induced seismicity has been reported (e.g. Baranova et al., 1999; Schultz et al., 2014). Such effects are not restricted to the reservoir alone; the country rock is affected too, in various styles, depending on the relative position (e.g. Segall, 1989).

6.1.5 S_{Hmax} calibration

The quantity and quality of the S_{Hmax} magnitude data are rather poor compared to the S_{hmin} magnitude data, but are very helpful to constrain the *best-fit* model. Otherwise only a linear *best-fit* function could be estimated. The two outliers (Fig. 14d) are the only two measured S_{Hmax} magnitude data from Kaiser et al. (1982) in a depth of 152 m in clay shale. As the measured in-situ data are more reasonable then the modelled magnitudes, the reason for the large deviation are most likely extrapolation problems close to the model surface, as discussed in the previous chapter.

6.2 Model variation

6.2.1 Impact of fault activation

The Great Slave Lake Shear Zone (GLS) and the Snowbird Tectonic Zone (STZ) are incorporated within the basement and the basin as vertical contact surfaces. The contact between the Alberta Basin and the foothills (foothill front), as well as the contact of the foothills to the Rocky Mountains (Rock Mountain front), are defined in the model as contact surfaces too. During the model calibration all these contact surfaces are handled as locked faults with a high friction coefficient. To test the impact of fault reactivation on the stress field we use in a model variant friction coefficients of 0.3 for STZ and GLS within the deeper basement. For the activation of the basement tectonic zones, the found correlation coefficient for S_{hmin} has been lowered only slightly: STZ alone ($r = 0.808$), GLS alone ($r = 0.828$) and STZ together with GLS ($r = 0.801$), compared to the *best-fit* model ($r = 0.835$). When the friction is lowered at the foothill front ($r = 0.836$) and the Rocky Mountains front ($r = 0.835$) alone, the correlation coefficient did not change. Only when both, the foothill and the Rocky Mountains front are active, the correlation declines ($r = 0.701$).

The S_{Hmax} orientation changes slightly (up to 2°) for all the fault activation. The exception is the Rocky Mountains front, where the $\widetilde{\Delta S}_{Hmax}$ orientation is equal to the *best-fit* model. This is expected, as only a few S_{Hmax} indicators are derived close to the Rock Mountains front.

6.2.2 Impact of Moho depth variation

To test the influence of the Moho topography (Fig. 5) on the stress state within the Alberta Basin, the *best-fit* model is modified. The Moho depth is uniform ($z = -50$ km) over the entire model region. The results of ΔS_{hmin} magnitudes show, that this model fits all data similar to the *best-fit* model ($r = 0.835$ for both model runs). S_{Hmax} orientation did not change between the models. Probably stress magnitudes and orientations are only slightly influenced by the Moho topography in this region.

6.3 Model application for deep geothermal reservoirs

To generate electricity, water with temperatures of 120–150 °C are needed. This requires well depths of 4000–6000 m in Alberta (Majorowicz and Grasby, 2010a, b). However, stimulation is required to enhance permeabilities (Enhanced Geothermal

Systems – EGS) in such depths. Furthermore, less hot water has the potential as a domestic heat source.

Three major issues for application of EGS are related to the crustal stresses. These are (1) the orientation of S_{Hmax}, as induced fractures opens parallel to S_{Hmax}. This is important for configuration of injection- and production wells. (2) The tectonic stress regime determine whether fractures open horizontally (thrust faulting) or vertically (strike slip and normal faulting regime). Furthermore, well stability is a major issue for deep and of cause very expensive wells, thus, (3) stress orientation and magnitude as well as differential stresses are important parameters for a save drilling.

S_{Hmax} orientations have been well understood in the Alberta Basin for decades (e.g. Bell and Gough, 1979; Bell et al., 1994; Fordjor et al., 1983; Reiter et al., 2014), mainly homogeneous in south-west to north-east orientation with the exception of the Peace River Arch and close to the Bow Island arch.

Horizontal wells, oriented parallel to S_{hmin} (south-east to north-west) (Bell and Grasby, 2012), with multiple fractures opens in S_{Hmax} direction. This creates several fluid propagation paths, which hast the potential to provide cost-efficient energy Hofmann et al. (2014).

We chose three locations in Alberta that have been identified as possible geothermal sites (Weides and Majorowicz, 2014; Pathak et al., 2013) and show S_{V}, S_{hmin} and S_{Hmax} along the virtual well path (Fig. 20). They are: (1) the Edson–Hinton region, with sediment thickness of 4000–6000 m and potentially temperatures of 100–150 °C, (2) the village Leduc, 30 km south of Edmonton, with the potential to heat houses (Weides and Majorowicz, 2014) and (3) the Hunt well site (e.g. Majorowicz et al., 2012) close to the town Fort McMurray, where heat is needed for industrial application (Pathak et al., 2013).

The virtual wells in Fig. 20 displays that thrust faulting regime occur close to the Rocky Mountains and foothills in shallow depths. Strike-slip regime is common within the basin from the surface to about 1500 to 3000 m depth and along the foothills between about 1000 to 4000 m depth. In greater depths from about 4500 m depth for the foothills, 3000 m depth for Edmonton and 2000 m depth for Fort McMurray, normal faulting regime is expected. This confirms Bell and Gough (1979); Bell et al. (1994); Bell and McLellan (1995); Bell and Babcock (1986); Bell and Bachu (2003); Bell and Grasby (2012); Woodland and Bell (1989); Fordjor et al. (1983); Jenkins and Kirkpatrick (1979). Therefore opening of induced fractures horizontally can be expected only close to the foothills, in depths less than 1000 m.

7 Conclusion

A large dataset of stress orientation and stress magnitude data are used to calibrate a 3-D geomechanical-numerical model of the Alberta Basin, which provide a good first order estimation of the contemporary stress tensor. During calibration procedure the density of the sediments, the orientation of the kinematic boundary conditions, and the magnitude of applied shortening of the model along the model boundaries are calibrated. As linear elastic material properties are used, magnitude of applied kinematic boundary conditions for the *best-fit* model can be determined by bivariate linear regression. This is based on only three (or more) models with variable boundary conditions. The stochastic verified calibration allows evaluating measurement outlier and systematic uncertainties. Variations of the *best-fit* model suggests, that main faults have only local effects on the stresses and the Moho topography has only negligible impact on the model results. A systematic drift of S_{hmin} magnitudes from leak-off test against the stress model is obvious, but may affected by multiple reasons.

The *best-fit* model applies for potential EGS reservoirs horizontal wells, oriented north-west to south-east. Virtual well path or cross estimation of the full contemporary stress tensors can be provided by the model in advance of any drilling. The model has potential to derive boundary conditions for local or reservoir models (e.g. Reiter et al., 2013), where petrological and tectonic inhomogeneities could be respected in more detail.

Acknowledgements. This study was conducted under the Helmholtz-Alberta-Initiative (HAI), which the first author is grateful for the financial support. We also want to thank the Alberta Geological Survey (AGS), in particular Kristine Haug, who allowed us to use the in-situ stress database. We thank Douglas Schmitt, Inga Moek, Dietrich Stromeyer and Tobias Hergert for fruitful discussions about stresses in the Alberta Basin, the modelling approach and technical support. Furthermore, we thank Nathaniel Walsh for spelling and grammar correction. Maps were generated using GMT software (Wessel et al., 2013).

The service charges for this open access publication have been covered by a Research Centre of the Helmholtz Association.

References

Adams, J. J.: Canadian Crustal Stress Data: A Compilation to 1987, Tech. rep., Geological Survey of Canada, 1987. 2427

Adams, J. J.: Crustal stresses in eastern Canada, in: Earthquakes at North-Atlantic Passive Margins: Neotectonics and Postglacial Rebound, edited by: Gregersen, S. R. and Basham, P. W., vol. 266, Springer, Netherlands, doi:10.1007/978-94-009-2311-9_17, 289–297, 1989. 2427

Adams, J. J. and Bell, J. S.: Crustal stresses in Canada, in: Neotectonics of North America, Decade of North American Neotectonics of North America, edited by: Slemmons, D. B. and Engdahl, E. R., Geological Society of America, doi:10.1007/978-94-009-2311-9_17, chap. 20, 367–386, 1991. 2427, 2438, 2439

Altmann, J. B., Müller, T. M., Müller, B. I., Tingay, M. R. P., and Heidbach, O.: Poroelastic contribution to the reservoir stress path, Int. J. Rock Mech. Min., 47, 1104–1113, doi:10.1016/j.ijrmms.2010.08.001, 2010. 2440

Amadei, B. and Stephansson, O.: Rock Stress and Its Measurement, Chapman & Hall, London, 1997. 2438

Anderson, E. M.: The Dynamics of Faulting and Dyke Formation with Application to Britain, 2nd edn., Oliver and Boyd, London, Edinburgh, 1951. 2438

Aulbach, S., Griffin, W., O'Reilly, S., and McCandless, T. E.: Genesis and evolution of the lithospheric mantle beneath the Buffalo Head Terrane, Alberta (Canada), Lithos, 77, 413–451, doi:10.1016/j.lithos.2004.04.020, 2004. 2431

Bachu, S., Haug, K., and Michael, K.: Stress Regime at Acid-Gas Injection Operations in Western Canada, ERCB/AGS Special Report 094, Energy Resources Conservation Board, 49, 2008. 2440, 2452, 2453

Baranova, V., Mustaqeem, A., and Bell, J. S.: A model for induced seismicity caused by hydrocarbon production in the Western Canada Sedimentary Basin, Can. J. Earth Sci., 36, 47–64, doi:10.1139/cjes-36-1-47, 1999. 2428, 2439, 2440, 2453

Barton, C. A. and Moos, D.: Geomechanical wellbore imaging: key to managing the asset life cycle, Tech. rep., GeoMechanics International, 2010. 2449

Bell, J. S.: Offset boreholes in the Rocky mountains of Alberta, Canada, Geology, 13, 734–737, doi:10.1130/0091-7613(1985)13<734:OBITRM>2.0.CO;2, 1985. 2439

Bell, J. S.: Attached and detached in-situ stress regimes in sedimentary basins, in: 55th EAEG Meeting, 1993. 2433

Bell, J. S.: In situ stresses in sedimentary rocks (part 1); measurement techniques, Geosc. Can., 23, 85–100, 1996a. 2441

Bell, J. S.: In situ stresses in sedimentary rocks (part 2): applications of stress measurements, Geosci. Can., 23, 135–153, 1996b. 2432, 2439, 2449

Bell, J. S. and Babcock, E. A.: The stress regime of the Western Canadian Basin and implications for hydrocarbon production, B. Can. Petrol. Geol., 34, 364–378, 1986. 2432, 2440, 2449, 2452, 2456

Bell, J. S. and Bachu, S.: In situ stress magnitude and orientation estimates for Cretaceous coal-bearing strata beneath the plains area of central and southern Alberta, B. Can. Petrol. Geol., 51, 1–28, doi:10.2113/gscpgbull.51.1.1, 2003. 2439, 2452, 2456

Bell, J. S. and Bachu, S.: In-situ stress magnitudes in the Alberta Basin-regional coverage for petroleum engineers, in: Proceedings of Canadian International Petroleum Conference, Society of Petroleum Engineers, Calgary, doi:10.2118/2004-155, 1–12, 2004. 2439, 2444, 2448

Bell, J. S. and Gough, D. I.: Northeast-southwest compressive stress in Alberta evidence from oil wells, Earth Planet. Sc. Lett., 45, 475–482, doi:10.1016/0012-821X(79)90146-8, 1979. 2438, 2439, 2449, 2451, 2455, 2456

Bell, J. S. and Gough, D.: Intraplate stress orientations from Alberta oil-wells, Geodynamics, 5, 96–104, doi:10.1029/GD005p0096, 1981. 2438

Bell, J. S. and Grasby, S. E.: The stress regime of the Western Canadian Sedimentary Basin, Geofluids, 12, 150–165, doi:10.1111/j.1468-8123.2011.00349.x, 2012. 2426, 2432, 2439, 2440, 2444, 2448, 2449, 2452, 2453, 2455, 2456

Bell, J. S. and McCallum, R.: In situ stress in the Peace River Arch area, Western Canada, B. Can. Petrol. Geol., 38, 270–281, 1990. 2432, 2449

Bell, J. S. and McLellan, P. J.: Exploration and production implications of subsurface rock stresses in western Canada, in: Proceedings of the Oil and Gas Forum, p. 5, 1995. 2425, 2439, 2452, 2456

Bell, J. S., Price, R. A., and McLellan, P. J.: In-situ stress in the Western Canada Sedimentary Basin, in: Geological Atlas of the Western Canada Sedimentary Basin, edited by: Mossop, G. D. and Shetsen, I., Canadian Society of Petroleum Geologists and Alberta Research Council, Alberta, chap. 29, 439–446, 1994. 2427, 2432, 2439, 2440, 2443, 2449, 2452, 2455, 2456

Boerner, D., Kurtz, R., Craven, J., Ross, G., and Jones, F.: A synthesis of electromagnetic studies in the Lithoprobe Alberta Basement Transect: constraints on Paleoproterozoic indentation tectonics, Can. J. Earth Sci., 37, 1509–1534, doi:10.1139/cjes-37-11-1509, 2000. 2431

Bouzidi, Y., Schmitt, D. R., Burwash, R. A., and Kanasewich, E. R.: Depth migration of deep seismic reflection profiles: crustal thickness variations in Alberta, Can. J. Earth Sci., 39, 331–350, doi:10.1139/e01-080, 2002. 2432, 2433, 2449

Brown, D. W.: Hot dry rock geothermal energy: important lessons from Fenton Hill, in: Thirty-Fourth Workshop on Geothermal Reservoir Engineering, Stanford, 3–6, 2009. 2425, 2427

Brown, E. and Hoek, E.: Trends in relationships between measured in-situ stresses and depth, Int. J. Rock Mech. Min., 15, 211–215, 1978. 2435

Brudy, M. and Kjørholt, H.: Stress orientation on the Norwegian continental shelf derived from borehole failures observed in high-resolution borehole imaging logs, Tectonophysics, 337, 65–84, doi:10.1016/S0040-1951(00)00299-7, 2001. 2449

Brudy, M., Zoback, M. D., Fuchs, K., Rummel, F., and Baumgärtner, J.: Estimation of the complete stress tensor to 8 km depth in the KTB scientific drill holes: Implications for crustal strength, J. Geophys. Res., 102, 18453–18475, 1997. 2436, 2483

Buchmann, T. J. and Connolly, P. T.: Contemporary kinematics of the Upper Rhine Graben: a 3-D finite element approach, Global Planet. Change, 58, 287–309, doi:10.1016/j.gloplacha.2007.02.012, 2007. 2426, 2436, 2447

Burianyk, M. J., Kanasewich, E. R., and Udey, N.: Broadside wide-angle seismic studies and three-dimensional structure of the crust in the southeast Canadian Cordillera, Can. J. Earth Sci., 34, 1156–1166, doi:10.1139/e17-093, 1997. 2433

Camelbeeck, T., de Viron, O., Van Camp, M., and Kusters, D.: Local stress sources in Western Europe lithosphere from geoid anomalies, Lithosphere, 5, 235–246, doi:10.1130/L238.1, 2013. 2428

Chacko, T., De, S. K., Creaser, R. A., and Muehlenbachs, K.: Tectonic setting of the Taltson magmatic zone at 1.9–2.0 Ga: a granitoid-based perspective, Can. J. Earth Sci., 37, 1597–1609, doi:10.1139/cjes-37-11-1597, 2000. 2431

Clowes, R. M., Burianyk, M. J., Gorman, A. R., and Kanasewich, E. R.: Crustal velocity structure from SAREX, the southern Alberta refraction experiment, Can. J. Earth Sci., 39, 351–373, doi:10.1139/E01-070, 2002. 2433

Coblentz, D. D. and Richardson, R. M.: Analysis of the South American intraplate stress field, J. Geophys. Res., 101, 8643, doi:10.1029/96JB00090, 1996. 2426

Corrigan, D., Hajnal, Z., Németh, B., and Lucas, S.: Tectonic framework of a Paleoproterozoic arc-continent to continent-continent collisional zone, Trans-Hudson Orogen, from geological and seismic reflection studies, Can. J. Earth Sci., 42, 421–434, doi:10.1139/E05-025, 2005. 2431

Dalton, C. a., Gaherty, J. B., and Courtier, A. M.: Crustal Vs structure in northwestern Canada: imaging the Cordillera-craton transition with ambient noise tomography, J. Geophys. Res., 116, B12315, doi:10.1029/2011JB008499, 2011. 2435, 2472

Duchane, D. and Brown, D.: Hot dry rock (HDR) geothermal energy research and development at Fenton Hill, New Mexico, Geo-Heat Centre Quarterly Bulletin, 23, 13–19, 2002. 2425, 2427

Dusseault, M. B. and Yassir, N. A.: Effects of rock anisotropy and heterogeneity on stress distributions at selected sites in North America, Eng. Geol., 37, 181–197, doi:10.1016/0013-7952(94)90055-8, 1994. 2432, 2449

Dyksterhuis, S., Albert, R., and Müller, R. D.: Finite-element modelling of contemporary and palaeo-intraplate stress using ABAQUS (TM), Comput. Geosci., 31, 297–307, doi:10.1016/j.cageo.2004.10.011, 2005. 2426

Eaton, D. W., Ross, G. M., and Hope, J.: The rise and fall of a cratonic arch: a regional seismic perspective on the Peace River Arch, Alberta, B. Can. Petrol. Geol., 47, 346–361, 1999. 2432, 2449

Edwards, S., Meredith, P., and Murrell, S.: An investigation of leak-off test data for estimating in-situ stress magnitudes: application to a basinwide study in the North Sea, in: Proceedings of SPE/ISRM Rock Mechchanics in Petroleum Engineering, Society of Petroleum Engineers, Trondheim, 8–10 July, doi:10.2118/47272-MS, 357–365, 1998. 2452

England, T. and Bustin, R.: Effect of thrust faulting on organic maturation in the southeastern Canadian Cordillera, Org. Geochem., 10, 609–616, 1986. 2439

English, J. M. and Johnston, S. T.: The Laramide Orogeny: what were the driving forces?, Int. Geol. Rev., 46, 833–838, doi:10.2747/0020-6814.46.9.833, 2004. 2432

Fernández-Viejo, G., and Clowes, R. M.: Lithospheric structure beneath the Archaean Slave Province and Proterozoic Wopmay orogen, northwestern Canada, from a lithoprobe refraction/wide-angle reflection survey, Geophys. J. Int., 153, 1–19, doi:10.1046/j.1365-246X.2003.01807.x, 2003. 2433

Fischer, K. and Henk, A.: A workflow for building and calibrating 3-D geomechanical models &ndash a case study for a gas reservoir in the North German Basin, Solid Earth, 4, 347–355, doi:10.5194/se-4-347-2013, 2013. 2426, 2447

Flesch, L. M., Holt, W. E., Haines, A. J., Wen, L., and Shen-Tu, B.: The dynamics of western North America: stress magnitudes and the relative role of gravitational potential energy, plate interaction at the boundary and basal tractions, Geophys. J. Int., 169, 866–896, doi:10.1111/j.1365-246X.2007.03274.x, 2007. 2437

Flowers, R. M., Ault, A. K., Kelley, S. A., Zhang, N., and Zhong, S.: Epeirogeny or eustasy? Paleozoic–Mesozoic vertical motion of the North American continental interior from thermochronometry and implications for mantle dynamics, Earth Planet. Sc. Lett., 317–318, 436–445, doi:10.1016/j.epsl.2011.11.015, 2012. 2431

Fordjor, C. K., Bell, J. S., and Gough, D. I.: Breakouts in Alberta and stress in the North American plate, Can. J. Earth Sci., 20, 1445–1455, doi:10.1139/e83-130, 1983. 2427, 2439, 2440, 2452, 2455, 2456

Fossen, H.: Structural Geology, Cambridge University Press, 2010. 2435, 2472

Fuchs, K. and Müller, B.: World stress map of the Earth: a key to tectonic processes and technological applications, Naturwissenschaften, 88, 357–371, doi:10.1007/s001140100253, 2001. 2425

SED
6, 2423–2494, 2014

Gabrielse, H. and Yorath, C.: The Cordilleran Orogen in Canada, Geosci. Can., 16, 67–83, 1989. 2432
Gardner, J. and Dumanoir, J.: Litho-density log interpretation, in: SPWLA 21st Annual Logging Symposium, Society of Petrophysicists and Well-Log Analysts, Lafayette, Louisiana, 1–23, 1980. 2441
Gay, N. C.: In-situ stress measurements in Southern Africa, Tectonophysics, 29, 447–459, doi:10.1016/0040-1951(75)90173-0, 1975. 2435
Ghosh, A., Holt, W. E., and Flesch, L. M.: Contribution of gravitational potential energy differences to the global stress field, Geophys. J. Int., 179, 787–812, doi:10.1111/j.1365-246X.2009.04326.x, 2009. 2428
Gough, D. I.: Mantle upflow under North America and plate dynamics, Nature, 311, 428–433, doi:10.1038/311428a0, 1984. 2439
Gough, D. I., Fordjor, C. K., and Bell, J. S.: A stress province boundary and tractions on the North American plate, Nature, 305, 619–621, doi:10.1038/305619a0, 1983. 2427, 2439
Grobe, M.: Distribution and thickness of salt within the Devonian Elk Point Group, Tech. rep., Alberta Energy and Utilities Board, Alberta Geological Survey, Edmonton, 2000. 2433, 2434
Gronseth, J. and Kry, P.: Instaneous shut-in pressure and its relationship to the minimum in-situ stress, in: Hydraulic Fracturing Stress Measurements, edited by: Zoback, M. D. and Haimson, B., US Nat. Comm. Rock Mechanics, Nat. Acad. Press, 55–60, 1983. 2442
Gu, Y. J., Okeler, A., Shen, L., and Contenti, S.: The Canadian Rockies and Alberta Network (CRANE): new constraints on the Rockies and Western Canada Sedimentary Basin, Seismol. Res. Lett., 82, 575, doi:10.1785/gssrl, 2011. 2433
Gunzburger, Y. and Magnenet, V.: Stress inversion and basement-cover stress transmission across weak layers in the Paris basin, France, Tectonophysics, 617, 44–57, doi:10.1016/j.tecto.2014.01.016, 2014. 2425
Haimson, B. C. and Cornet, F.: ISRM Suggested Methods for rock stress estimation – Part 3: hydraulic fracturing (HF) and/or hydraulic testing of pre-existing fractures (HTPF), Int. J. Rock Mech. Min., 40, 1011–1020, doi:10.1016/j.ijrmms.2003.08.002, 2003. 2441
Haimson, B. C. and Fairhurst, C.: In-situ stress determination at great depth by means of hydraulic fracturing, in: The 11th US Symposium on Rock Mechechanics (USRMS), Berkeley, California, 16–19 June, American Rock Mechchanics Association, 559–584, 1969. 2442
Hajnal, Z., Lewry, J., White, D. J., Ashton, K. E., Clowes, R. M., Stauffer, M., Gyorfi, I., and Takacs, E.: The Sask Craton and Hearne Province margin: seismic reflection studies in the

SED
6, 2423–2494, 2014

Calibration of 3-D crustal stress model Alberta Basin

K. Reiter and O. Heidbach

western Trans-Hudson Orogen, Can. J. Earth Sci., 42, 403–419, doi:10.1139/E05-026, 2005. 2431
Halchuk, S. and Mereu, R.: A seismic investigation of the crust and Moho underlying the Peace River Arch, Canada, Tectonophysics, 185, 1–19, doi:10.1016/0040-1951(90)90401-S, 1990. 2432, 2433, 2449
Hamilton, W., Langenberg, C., Price, M., and Chao, D.: Geological Map of Alberta, Tech. rep., Alberta Geological Survey, Edmonton, 1999. 2477
Hawkes, C. D., Bachu, S., Haug, K., and Thompson, A. W.: Analysis of in-situ stress regime in the Alberta Basin, Canada, for performance assessment of CO_2 geological sequestration sites, in: Proceedings of the Fourth Annual Conference on Carbon Capture and Sequestration DOE/NETL, p. 22, 2005. 2440
Heidbach, O., Reinecker, J., Tingay, M. R. P., Müller, B., Sperner, B., Fuchs, K., and Wenzel, F.: Plate boundary forces are not enough: second- and third-order stress patterns highlighted in the World Stress Map database, Tectonics, 26, 1–19, doi:10.1029/2007TC002133, 2007. 2427, 2449
Heidbach, O., Tingay, M. R. P., Barth, A., Reinecker, J., Kurfeß, D., and Müller, B.: Global crustal stress pattern based on the World Stress Map database release 2008, Tectonophysics, 482, 3–15, doi:10.1016/j.tecto.2009.07.023, 2010. 2427
Heidbach, O., Hergert, T., Reinecker, J., Reiter, K., Giger, S., Vietor, T., and Marschall, P.: In situ stress in Switzerland – from pointwise field data to a 3-D continuous quantification, in: International Workshop on Geomechanics and Energy – The Ground as Energy Source and Storage, EAGE, Lausanne, doi:10.3997/2214-4609.20131977, 1–4, 2013. 2425, 2426, 2447
Heim, A.: Untersuchungen über den Mechanismus der Gebirgsbildung: im Anschluss an die geologische Monographie der Tödi-Windgällen-Gruppe, Benno Schwabe Verlagsbuchhandlung, Basel, 1878. 2435, 2483
Henk, A.: Pre-drilling prediction of the tectonic stress field with geomechanical models, first break, 23, 53–57, 2005. 2426
Henton, J. A., Craymer, M. R., Ferland, R., Dragert, H., Mazzotti, S., and Forbes, D. L.: Crustal motion and deformation monitoring of the Canadian landmass, Geomatica, 60, 173–191, 2006. 2432, 2436, 2437
Hergert, T. and Heidbach, O.: Geomechanical model of the Marmara Sea region-II. 3-D contemporary background stress field, Geophys. J. Int., 185, 1090–1102, doi:10.1111/j.1365-246X.2011.04992.x, 2011. 2426, 2436, 2447

SED
6, 2423–2494, 2014

Calibration of 3-D crustal stress model Alberta Basin

K. Reiter and
O. Heidbach

Hickman, S. and Zoback, M. D.: Stress orientations and magnitudes in the SAFOD pilot hole, Geophys. Res. Lett., 31, L15S12, doi:10.1029/2004GL020043, 2004. 2483

Hoffman, P. F.: Precambrian geology and tectonic history of North America, in: The Geology of North America, The Geological Society of America, 447–512, 1989. 2431

Hofmann, H., Weides, S., Babadagli, T., Zimmermann, G., Moeck, I., Majorowicz, J., and Unsworth, M.: Potential for enhanced geothermal systems in Alberta, Canada, Energy, 69, 578–591, doi:10.1016/j.energy.2014.03.053, 2014. 2426, 2455

Hubbert, M. K. and Willis, D. G.: Mechanics of hydraulic fracturing, AIME Trans, 210, 153–168, 1957. 2441

Humphreys, E. D. and Coblentz, D. D.: North American dynamics and western U. S. tectonics, Rev. Geophys., 45, 30, doi:10.1029/2005RG000181, 2007. 2426, 2428

Hyndman, R. D., Currie, C. A., Mazzotti, S., and Frederiksen, A.: Temperature control of continental lithosphere elastic thickness, Te vs Vs, Earth Planet. Sc. Lett., 277, 539–548, doi:10.1016/j.epsl.2008.11.023, 2009. 2432

Jaeger, J., Cook, N., and Zimmerman, R.: Fundamentals of Rock Mechechanics, John Wiley & Sons, 2009. 2438, 2450

Jarosinski, M., Beekman, F., Bada, G., and Cloetingh, S.: Redistribution of recent collision push and ridge push in Central Europe: insights from FEM modelling, Geophys. J. Int., 167, 860–880, doi:10.1111/j.1365-246X.2006.02979.x, 2006. 2426

Jenkins, G. and Kirkpatrick, J.: Mbustion Project, J. Can. Petrol. Technol., 18, 85–94, doi:10.2118/79-02-07, 1979. 2440, 2452, 2456

Kaiser, P., Mackay, C., and Morgenstern, N.: Performance of a shaft in weak rock (Bearpa W Shale), in: ISRM International Symposium, Aachen, Germany, 26–28 May, 613–622, 1982. 2443, 2453

Kanamori, H. and Brodsky, E. E.: The physics of earthquakes, Rep. Prog. Phys., 67, 1429–1496, doi:10.1088/0034-4885/67/8/R03, 2004. 2438

King, M.: Static and dynamic elastic properties of rocks from the Canadian Shield, Int. J. Rock Mech. Min., 20, 237–241, 1983. 2435

Kry, P. and Gronseth, J.: In-situ stresses and hydraulic fracturing in the Deep Basin, J. Can. Petrol. Technol., 22, 31–35, doi:10.2118/83-06-02, 1983. 2452

Leckie, D. A. and Smith, D. G.: Regional setting, evolution, and depositional cycles of the Western Canada Foreland Basin, in: Foreland Basins and Fold Belts, edited by: Macqueen, R. W.

and Leckie, D. A., vol. A136, American Association of Petroleum Geologists, chap. 1, 9–46, 1992. 2432

Legarth, B., Huenges, E., and Zimmermann, G.: Hydraulic fracturing in a sedimentary geothermal reservoir: results and implications, Int. J. Rock Mech. Min., 42, 1028–1041, doi:10.1016/j.ijrmms.2005.05.014, 2005. 2425

Li, G., Lorwongngam, A., and Roegiers, J.: Critical review of leak-off test as a practice for determination of in-situ stresses, in: 43rd US Rock Mechchanics Symposium and 4th US-Canada Rock Mechanics Symposium, American Rock Mechanics Association, Asheville, p. 5, 2009. 2441

Lindner, E. N. and Halpern, J. A.: In-situ stress in north America: a compilation, Int. J. Rock Mech. Min., 15, 183–203, 1978. 2483

Ljunggren, C., Chang, Y., Janson, T., and Christiansson, R.: An overview of rock stress measurement methods, Int. J. Rock Mech. Min., 40, 975–989, doi:10.1016/j.ijrmms.2003.07.003, 2003. 2425, 2441

Majorowicz, J. and Grasby, S. E.: Heat flow, depth–temperature variations and stored thermal energy for enhanced geothermal systems in Canada, J. Geophys. Eng., 7, 232–241, doi:10.1088/1742-2132/7/3/002, 2010a. 2426, 2454

Majorowicz, J. and Grasby, S. E.: High potential regions for enhanced geothermal systems in Canada, Nat. Resour. Res., 19, 177–188, doi:10.1007/s11053-010-9119-8, 2010b. 2426, 2454

Majorowicz, J., Gosnold, W., Gray, A. D., Safanda, J., Klenner, R., and Unsworth, M. J.: Implications of post-glacial warming for northern Alberta heat flow-correcting for the underestimate of the geothermal potential, Geoth. Res. T., 36, 693–698, 2012. 2455

Mallet, J.-L.: Discrete smooth interpolation in geometric modelling, Comput. Aided Design, 24, 178–191, doi:10.1016/0010-4485(92)90054-E, 1992. 2433, 2434

Mavko, G., Mukerji, T., and Dvorkin, J.: The Rock Physics Handbook: Tools for Seismic Analysis of Porous Media, Cambridge University Press, Cambridge, 2009. 2435

Mazzotti, S., Leonard, L. J., Cassidy, J. F., Rogers, G. C., and Halchuk, S.: Seismic hazard in western Canada from GPS strain rates versus earthquake catalog, J. Geophys. Res., 116, B12310, doi:10.1029/2011JB008213, 2011. 2432, 2436, 2437

McGarr, A. and Gay, N. C.: State of stress in the earth's crust, Annu. Rev. Earth Pl. Sc., 6, 405–436, 1978. 2438, 2443, 2450

McLellan, P.: In-situ stress prediction and measurement by hydraulic fracturing, Wapiti, Alberta, in: Proceedings of Annual Technical Meeting, Society of Petroleum Engineers, Calgary, doi:10.2118/87-38-58, 967–933, 1987. 2442

Meijer Drees, N. C.: Devonian Elk Point Group of the Western Canada Sedimentary Basin, in: Geological Atlas of the Western Canada Sedimentary Basin, edited by: Mossop, G. D. and Shetsen, I., Canadian Society of Petroleum Geologists and Alberta Research Council, Alberta, chap. 10, 129–147, 1994. 2433

Mossop, G. D. and Shetsen, I. (Eds.): Geological Atlas of the Western Canada Sedimentary Basin, Canadian Society of Petroleum Geologists and Alberta Research Council, 1994a. 2431, 2434

Mossop, G. D. and Shetsen, I.: Introduction to the geological atlas of the Western Canada Sedimentary Basin, in: Geological Atlas of the Western Canada Sedimentary Basin, edited by: Mossop, G. D. and Shetsen, I., Canadian Society of Petroleum Geologists and Alberta Research Council, Alberta, chap. 1, 1–11, 1994b. 2433

Müller, B., Wehrle, V., Zeyen, H., and Fuchs, K.: Short-scale variations of tectonic regimes in the western European stress province north of the Alps and Pyrenees, Tectonophysics, 275, 199–219, doi:10.1016/S0040-1951(97)00021-8, 1997. 2427

Naliboff, J., Lithgow-Bertelloni, C., Ruff, L., and de Koker, N.: The effects of lithospheric thickness and density structure on Earth's stress field, Geophys. J. Int., 188, 1–17, doi:10.1111/j.1365-246X.2011.05248.x, 2012. 2428

Németh, B., Hajnal, Z., and Lucas, S.: Moho signature from wide-angle reflections: preliminary results of the 1993 Trans-Hudson Orogen refraction experiment, Tectonophysics, 264, 111–121, doi:10.1016/S0040-1951(96)00121-7, 1996. 2433

Németh, B., Clowes, R. M., and Hajnal, Z.: Lithospheric structure of the Trans-Hudson Orogen from seismic refraction – wide-angle reflection studies, Can. J. Earth Sci., 42, 435–456, doi:10.1139/e05-032, 2005. 2431, 2433

Nurkowski, J. R.: Coal quality, coal rank variation and its relation to reconstructed overburden, upper cretaceous and tertiary plains coals, Alberta, Canada, AAPG Bull., 68, 285–295, 1984. 2439

Obert, L.: In situ determination of stress in rock, Min. Eng.-Littleton, 14, 51–58, 1962. 2443

Okrusch, M. and Matthes, S.: Mineralogie, Springer-Lehrbuch, Springer-Verlag, Berlin, Heidelberg, doi:10.1007/b139038, 2005. 2435, 2472

Orlic, B. and Wassing, B. B. T.: A study of stress change and fault slip in producing gas reservoirs overlain by elastic and viscoelastic caprocks, Rock Mech. Rock Eng., 46, 421–435, doi:10.1007/s00603-012-0347-6, 2012. 2426

Parsons, T.: Tectonic stressing in California modeled from GPS observations, J. Geophys. Res., 111, 1–16, doi:10.1029/2005JB003946, 2006. 2426

Pathak, V., Babadagli, T., Majorowicz, J. A., and Unsworth, M. J.: Evaluation of engineered geothermal systems as a heat source for oil sands production in Northern Alberta, Nat. Resour. Res., 23, 247–265, doi:10.1007/s11053-013-9218-4, 2013. 2455

Peska, P. and Zoback, M. D.: Compressive and tensile failure of inclined well bores and determination of in situ stress and rock strength, J. Geophys. Res., 100, 12791, doi:10.1029/95JB00319, 1995. 2425

Podruski, J.: Contrasting character of the Peace River and Sweetgrass arches, Western Canada Sedimentary Basin, Geosci. Can., 15, 94–97, 1988. 2450

Porter, J. W., Price, R. A., and McCrossan, R. G.: The Western Canada Sedimentary Basin, Philos. T. R. Soc. Lond., 305, 169–192, 1982. 2431

Poulton, T., Christopher, J., Hays, B., Losert, J., Tittemore, J., and Gilchrist, R.: Jurassic and lowermost Cretaceous Strata of the Western Canada Sedimentary Basin, in: Geological Atlas of the Western Canada Sedimentary Basin, edited by: Mossop, G. D. and Shetsen, I., Canadian Society of Petroleum Geologists and Alberta Research Council, Alberta, chap. 18, 297–316, 1994. 2431

Price, R. A.: The Cordilleran foreland thrust and fold belt in the southern Canadian Rocky Mountains, Geol. Soc. Spec. Publ., 9, 427–448, doi:10.1144/GSL.SP.1981.009.01.39, 1981. 2431

Price, R. A.: Cordilleran tectonics and the evolution of the Western Canada Sedimentary Basin, in: Geological Atlas of the Western Canada Sedimentary Basin, edited by: Mossop, G. D. and Shetsen, I., Canadian Society of Petroleum Geologists and Alberta Research Council, chap. 2, 13–24, 1994. 2433

Reiter, K., Heidbach, O., and Moeck, I.: Stress field modelling in the Alberta Basin, Canada, in: International Workshop on Geomechanics and Energy – The Ground as Energy Source and Storage, EAGE, Lausanne, doi:10.3997/2214-4609.20131973, 26–28, 2013. 2456

Reiter, K., Heidbach, O., Schmitt, D. R., Haug, K., Ziegler, M., and Moeck, I.: A revised crustal stress orientation database for Canada, Tectonophysics, in press, 2014. 2427, 2432, 2439, 2441, 2449, 2455, 2485

Richardson, R. M.: Ridge forces, absolute plate motions, and the intraplate stress field, J. Geophys. Res., 97, 11739–11748, doi:10.1029/91JB00475, 1992. 2427

Ristau, J., Rogers, G. C., and Cassidy, J. F.: Stress in western Canada from regional moment tensor analysis, Can. J. Earth Sci., 44, 127–148, doi:10.1139/e06-057, 2007. 2439

Roche, V., Homberg, C., and Rocher, M.: Fault nucleation, restriction, and aspect ratio in layered sections: quantification of the strength and stiffness roles using numerical modeling, J. Geophys. Res.-Sol. Ea., 118, 4446–4460, doi:10.1002/jgrb.50279, 2013. 2425, 2452

Röckel, T. and Lempp, C.: Der Spannungszustand im Norddeutschen Becken, Erdöl Erdgas Kohle, 119, 73–80, 2003. 2425, 2433

Ross, G. M., Broome, J., and Miles, W.: Potential fields and basement structure – Western Canada Sedimentary Basin, in: Geological Atlas of the Western Canada Sedimentary Basin, edited by: Mossop, G. D. and Shetsen, I., Canadian Society of Petroleum Geologists and Alberta Research Council, Alberta, chap. 4, 41–47, 1994. 2431

Ross, G. M., Eaton, D. W., Boerner, D. E., and Miles, W.: Tectonic entrapment and its role in the evolution of continental lithosphere: an example from the Precambrian of western Canada, Tectonics, 19, 116–134, doi:10.1029/1999TC900047, 2000. 2431

Roth, F. and Fleckenstein, P.: Stress orientations found in north-east Germany differ from the West European trend, Terra Nova, 13, 289–296, doi:10.1046/j.1365-3121.2001.00357.x, 2001. 2425, 2433

Sami, T. T. and James, N. P.: Evolution of an early Proterozoic foreland basin carbonate platform, lower Pethei Group, Great Slave Lake, north-west Canada, Sedimentology, 40, 403–430, doi:10.1111/j.1365-3091.1993.tb01343.x, 1993. 2431

Sbar, M. L. and Sykes, L. R.: Contemporary compressive stress and seismicity in eastern North America: an example of intra-plate tectonics, Geol. Soc. Am. Bull., 84, 1861–1882, doi:10.1130/0016-7606(1973)84<1861:CCSASI>2.0.CO;2, 1973. 2427, 2439

Schmitt, D. R., Currie, C. A., and Zhang, L.: Crustal stress determination from boreholes and rock cores: fundamental principles, Tectonophysics, 580, 1–26, doi:10.1016/j.tecto.2012.08.029, 2012. 2425, 2438, 2441, 2443, 2450

Schultz, R., Stern, V., and Gu, Y. J.: An investigation of seismicity clustered near the Cordel Field, west-central Alberta and its relation to a nearby disposal well, J. Geophys. Res.-Sol. Ea., 119, 1–14, doi:10.1002/2013JB010836, 2014. 2428, 2453

Segall, P.: Earthquakes triggered by fluid extraction, Geology, 17, 942–946, 1989. 2453

Sheorey, P.: A theory for in situ stresses in isotropic and transverseley isotropic rock, Int. J. Rock Mech. Min., 31, 23–34, doi:10.1016/0148-9062(94)92312-4, 1994. 2436, 2483
Shragge, J., Bostock, M. G., Bank, C.-G., and Ellis, R. M.: Integrated teleseismic studies of the southern Alberta upper mantle, Can. J. Earth Sci., 39, 399–411, doi:10.1139/e01-084, 2002. 2433
Smith, D.: Paleogeographic evolution of the Western Canada Foreland Basin, in: Geological Atlas of the Western Canada Sedimentary Basin, edited by: Mossop, G. D. and Shetsen, I., Canadian Society of Petroleum Geologists and Alberta Research Council, Alberta, chap. 17, 227–296, 1994. 2431
Spence, G. D. and McLean, N. A.: Crustal seismic velocity and density structure of the Intermontane and Coast belts, southwestern Cordillera, Can. J. Earth Sci., 35, 1362–1379, doi:10.1139/cjes-35-12-1362, 1998. 2433
Tingay, M. R. P., Müller, B., Reinecker, J., Heidbach, O., Wenzel, F., and Fleckenstein, P.: Understanding tectonic stress in the oil patch: the World Stress Map project, The Leading Edge, 24, 1276–1282, doi:10.1190/1.2149653, 2005. 2427, 2433
Turcotte, D. L. and Schubert, G.: Geodynamics, Cambridge University Press, 2002. 2435, 2472
USGS: GTOPO30 – Global Land Survey Digital Elevation Model (GLSDEM), available at: https://lta.cr.usgs.gov/GTOPO30, 2008. 2434
Van Wees, J. D., Orlic, B., Van Eijs, R., Zijl, W., Jongerius, P., Schreppers, G. J., Hendriks, M., and Cornu, T.: Integrated 3-D geomechanical modelling for deep subsurface deformation: a case study of tectonic and human-induced deformation in the eastern Netherlands, Geol. Soc. Spec. Publ., 212, 313–328, doi:10.1144/GSL.SP.2003.212.01.21, 2003. 2426
Wang, Z., Nur, A., and Ebrom, D.: Seismic and Acoustic Velocities in Reservoir Rocks: Volume 3, Recent Developments, Expl. Geophys, 3, 2000. 2435
Warpinski, N.: Determining the minimum in situ stress from hydraulic fracturing through perforations, Int. J. Rock Mech. Min., 26, 523–531, doi:10.1016/0148-9062(89)91430-7, 1989. 2425, 2452
Weides, S. and Majorowicz, J.: Implications of spatial variability in heat flow for geothermal resource evaluation in large foreland basins: the case of the Western Canada Sedimentary Basin, Energies, 7, 2573–2594, doi:10.3390/en7042573, 2014. 2455
Weides, S., Moeck, I., Majorowicz, J., Palombi, D., Grobe, M., and Mareschal, J.-C.: Geothermal exploration of Paleozoic formations in Central Alberta, Can. J. Earth Sci., 50, 519–534, doi:10.1139/cjes-2012-0137, 2013. 2426

SED
6, 2423–2494, 2014

Weides, S., Moeck, I., Majorowicz, J., and Grobe, M.: The Cambrian Basal Sandstone Unit in central Alberta – an investigation of temperature distribution, petrography and hydraulic and geomechanical properties of a deep saline aquifer, Can. J. Earth Sci., doi:10.1139/cjes-2014-0011, 2014. 2426

Welford, J. K., Clowes, R. M., Ellis, R. M., Spence, G. D., Asudeh, I., and Hajnal, Z.: Lithospheric structure across the craton-Cordilleran transition of northeastern British Columbia, Can. J. Earth Sci., 38, 1169–1189, doi:10.1139/cjes-38-9-1169, 2001. 2433

Wessel, P., Smith, W. H. F., Scharroo, R., Luis, J., and Wobbe, F.: Generic mapping tools: improved version released, Eos T. Am. Geophys. Un., 94, 409–410, doi:10.1002/2013EO450001, 2013. 2457

Wessling, S., Junker, R., Rutqvist, J., Silin, D., Sulzbacher, H., Tischner, T., and Tsang, C.-F.: Pressure analysis of the hydromechanical fracture behaviour in stimulated tight sedimentary geothermal reservoirs, Geothermics, 38, 211–226, doi:10.1016/j.geothermics.2008.10.003, 2009. 2425

White, A. J., Traugott, M. O., and Swarbrick, R. E.: The use of leak-off tests as means of predicting minimum in-situ stress, Petrol. Geosci., 8, 189–193, doi:10.1144/petgeo.8.2.189, 2002. 2441, 2442, 2452

White, D. J., Thomas, M., Jones, A., Hope, J., Németh, B., and Hajnal, Z.: Geophysical transect across a Paleoproterozoic continent continent collision zone: the Trans-Hudson Orogen, Can. J. Earth Sci., 42, 385–402, doi:10.1139/E05-002, 2005. 2434, 2472

Woodland, D. and Bell, J. S.: In situ stress magnitudes from mini-frac records in Western Canada, J. Can. Petrol. Technol., 28, 22–31, doi:10.2118/89-05-01, 1989. 2439, 2440, 2442, 2452, 2456

Wright, G., McMechan, M., and Potter, D.: Structure and architecture of the Western Canada Sedimentary Basin, in: Geological Atlas of the Western Canada Sedimentary Basin, edited by: Mossop, G. D. and Shetsen, I., Canadian Society of Petroleum Geologists and Alberta Research Council, chap. 3, 25–40, 1994. 2431, 2433, 2476

Yassir, N. A. and Bell, J. S.: Relationships between pore pressure, stresses, and present-day geodynamics in the Scotian Shelf, offshore eastern Canada, AAPG Bull., 78, 1863–1880, 1994. 2425

Zang, A. and Stephansson, O.: Stress Field of the Earth's Crust, Springer Netherlands, Dordrecht, doi:10.1007/978-1-4020-8444-7, 2010. 2425, 2438, 2441

Zelt, C. A. and White, D. J.: Crustal structure and tectonics of the southeastern Canadian Cordillera, J. Geophys. Res., 100, 24255, doi:10.1029/95JB02632, 1995. 2433

Zhou, S.: A method of estimating horizontal principal stress magnitudes from stress-induced wellbore breakout and leak-off tests and its application to petroleum engineering, Petrol. Geosci., 3, 57–64, 1997. 2441

Zoback, M. D.: Reservoir Geomechanics: Earth Stress and Rock Mechanics Applied to Exploration, Production and Wellbore Stability, Cambridge Press, 2007. 2438

Zoback, M. D. and Zoback, M. L.: State of stress and intraplate earthquakes in the United States, Science, 213, 96–104, doi:10.1126/science.213.4503.96, 1981. 2427

Zoback, M. D. and Zoback, M. L.: Tectonic stress field of North America and relative plate motions, in: Neotectonics of North America, edited by: Slemmons, D. B. and Engdahl, E. R., Geological Society of America, 339–366, 1991. 2427

Zoback, M. D., Barton, C., Brudy, M., Castillo, D., Finkbeiner, T., Grollimund, B., Moos, D., Peska, P., Ward, C., and Wiprut, D.: Determination of stress orientation and magnitude in deep wells, Int. J. Rock Mech. Min., 40, 1049–1076, doi:10.1016/j.ijrmms.2003.07.001, 2003. 2441

Zoback, M. L.: First- and second-order patterns of stress in the lithosphere: the World Stress Map project, J. Geophys. Res., 97, 11703–11728, doi:10.1029/92JB00132, 1992. 2427

Zoback, M. L. and Mooney, W. D.: Lithospheric buoyancy and continental intraplate stresses, Int. Geol. Rev., 45, 95–118, doi:10.2747/0020-6814.45.2.95, 2003. 2427

Zoback, M. L. and Zoback, M. D.: State of stress in the conterminous United States, J. Geophys. Res., 85, 6113–6156, 1980. 2427, 2439

Zoback, M. L. and Zoback, M. D.: Tectonic stress field of the continental United States, in: Geophysical Framework of the Continental United States, edited by: Pakiser, L. and Mooney, W. D., vol. 172, Geological Society of America, geological edn., doi:10.1130/MEM172-p523, chap. 24, 523–540, 1989. 2427

Zoback, M. L., Zoback, M. D., Adams, J. J., Assumpção, M., Bell, J. S., Bergman, E. A., Blümling, P., Brereton, N. R., Denham, D., Ding, J., Fuchs, K., Gay, N., Gregersen, S., Gupta, H. K., Gvishiani, A., Jacob, K., Klein, R., Knoll, P., Magee, M., Mercier, J. L., Müller, B. C., Paquin, C., Rajendran, K., Stephansson, O., Suarez, G., Suter, M., Udias, A., Xu, Z. H., and Zhizhin, M.: Global patterns of tectonic stress, Nature, 341, 291–298, doi:10.1038/341291a0, 1989. 2427

SED
6, 2423–2494, 2014

Calibration of 3-D crustal stress model Alberta Basin

K. Reiter and O. Heidbach

Table 1. Material properties of the Alberta model.

Lithology	Density ($kg\,m^{-3}$)	Young's modulus (Pa)	Poisson's ratio
Sediments	2200[a]	6.0×10^{10}[b]	0.15[b]
Rock Salt	2100[c]	4.0×10^{10}[d]	0.38[d]
Foothills	2400[b]	6.0×10^{10}[b]	0.20[b]
Rocky Mnts.	2500[b]	6.0×10^{10}[b]	0.20[b]
Basement	2800[e]	7.0×10^{10}[f]	0.21[f]
Mantle	3350[e]	1.5×10^{11}[b]	0.25[b]

[a] *Best-fit* (tested during calibration)
[b] Estimated based on Turcotte and Schubert (2002)
[c] Okrusch and Matthes (2005)
[d] Fossen (2010)
[e] White et al. (2005)
[f] Calculated based on Dalton et al. (2011).

SED
6, 2423–2494, 2014

K. Reiter and O. Heidbach

Table 2. Overview about major push-and-pull experiments. The orientation of the kinematic boundary condition is indicated in Fig. 4. Four test scenarios with different push and pulls magnitudes are displayed, same as in Fig. 15a and b. The kinematic boundary conditions for the *best-fit* model (last line) are calculated based on bivariate linear regression, see text.

Models	push from SW [m]	pull to SE [m]	median ΔS_{hmin} [MPa]	median ΔS_{Hmax} [MPa]
test scenarios	0.00	150.00	−1.120	7.246
	200.00	100.00	−6.424	−10.800
	200.00	250.00	1.264	−9.561
	−50.00	−280.00	6.273	12.705
best-fit	86.24	194.52	−0.005	0.018

SED
6, 2423–2494, 2014

Calibration of 3-D crustal stress model Alberta Basin

K. Reiter and
O. Heidbach

Table A1. Notation.

ν	Poisson's ratio
$\boldsymbol{\epsilon}$	Strain
ρ	Density
$\boldsymbol{\sigma}$	Stress at a point
$\hat{\boldsymbol{\sigma}}$	Principal stress
$\sigma_1, \sigma_2, \sigma_3$	largest, middle and least principal stress
E	Young's Modulus
k	k ratio ($S_{\mathrm{Hmean}}/S_{\mathrm{V}}$)
S_{V}	Vertical stress
S_{Hmax}	Maximum horizontal stress
S_{hmin}	Minimum horizontal stress
S_{Hmean}	Mean horizontal stress
ΔS	deviation between S_{measured} and S_{model}
$n\Delta S$	ΔS normalized by S_{model}
$\widetilde{\Delta S}$	whole model median of ΔS
$\overline{\Delta S}$	whole model mean of ΔS

SED

6, 2423–2494, 2014

Calibration of 3-D crustal stress model Alberta Basin

K. Reiter and O. Heidbach

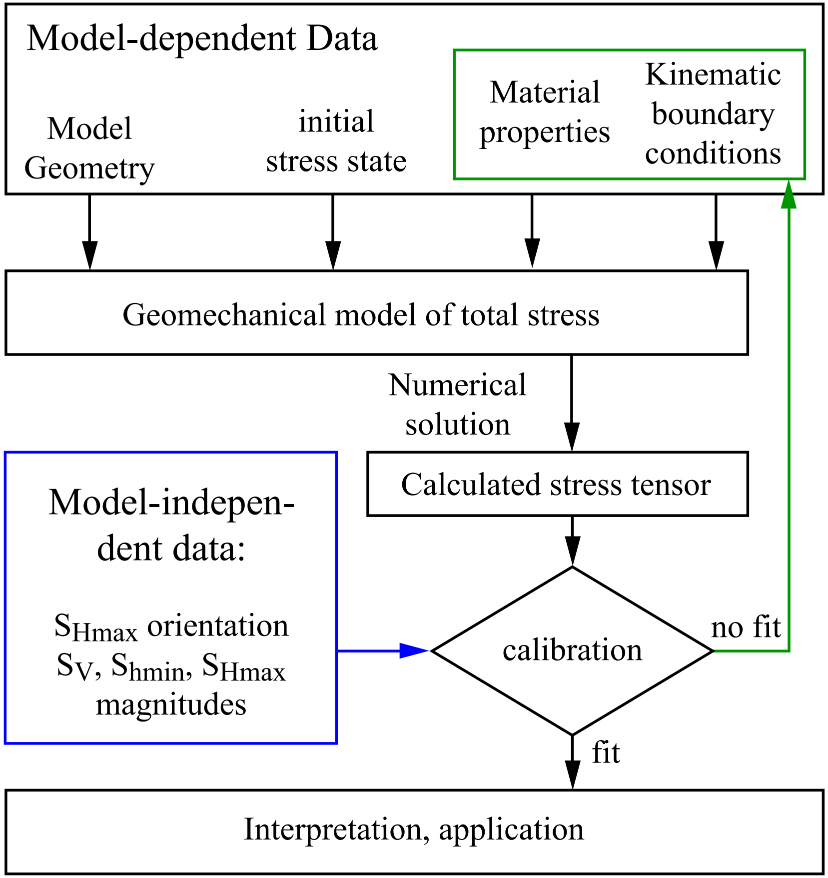

Figure 1. Sketch of the general workflow. The geomechanical model is prepared based on the model geometry, the material properties, the variable kinematic boundary conditions and the initial stress state. The numerically modelled total stress tensor is calibrated on model independent in-situ stress data until the model fits the calibration data.

SED
6, 2423–2494, 2014

K. Reiter and
O. Heidbach

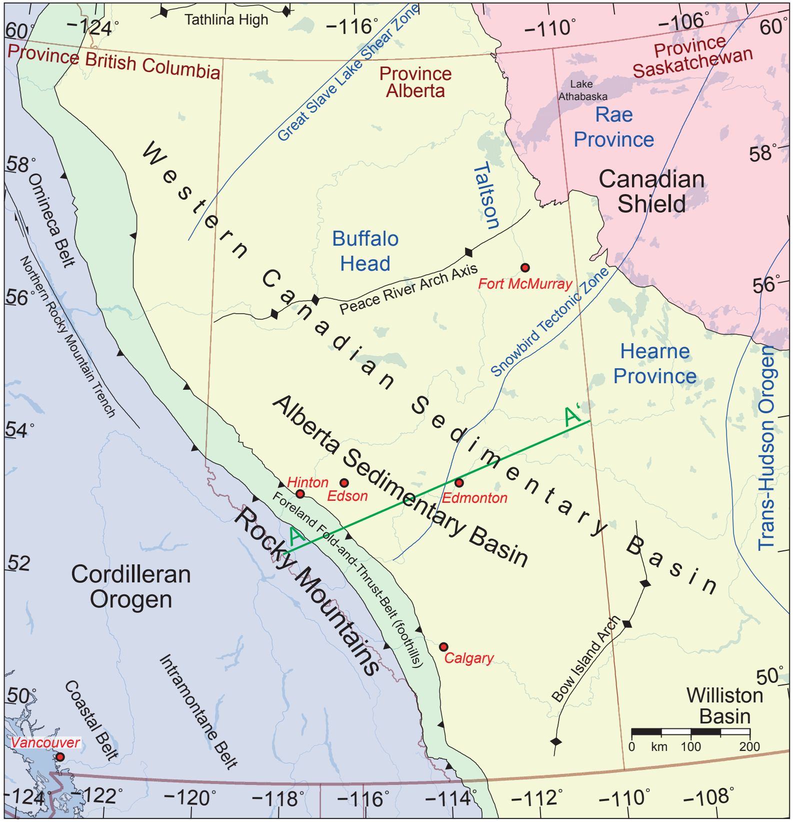

Figure 2. Tectonic map of Alberta and surroundings displaying the important structural features. Blue lines and labels indicate Precambrian structures in the basement. Provincial boundaries and areas are indicated by reddish-brown colours and tectonic features are labeled in black. The trace of the cross section in Fig. 3 is indicated by a green line. The map is modified and redrawn after Wright et al. (1994).

SED
6, 2423–2494, 2014

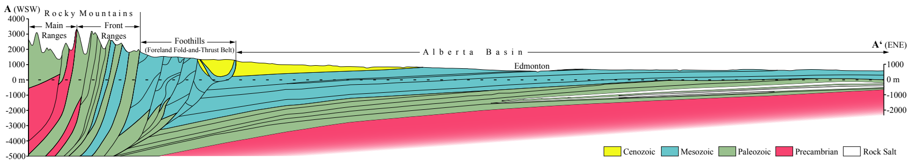

Figure 3. Cross section across Alberta in west-southwest to east-northeast orientation; the trace is highlighted in Figs. 2 and 4. Visible is the Alberta Basin as a wedge shaped retro-arc foreland basin, together with parts of the Rocky Mountains and the foreland fold-and-thrust belt (foothills) in between. The rock units are roughly indicated by the stratigraphic age. Additional thick rock salt units indicated separately, because of their potential to detach the stress field. The vertical exaggeration is 10 times, redrawn after Hamilton et al. (1999).

Discussion Paper | Discussion Paper | Discussion Paper | Discussion Paper |

SED
6, 2423–2494, 2014

Calibration of 3-D crustal stress model Alberta Basin

K. Reiter and O. Heidbach

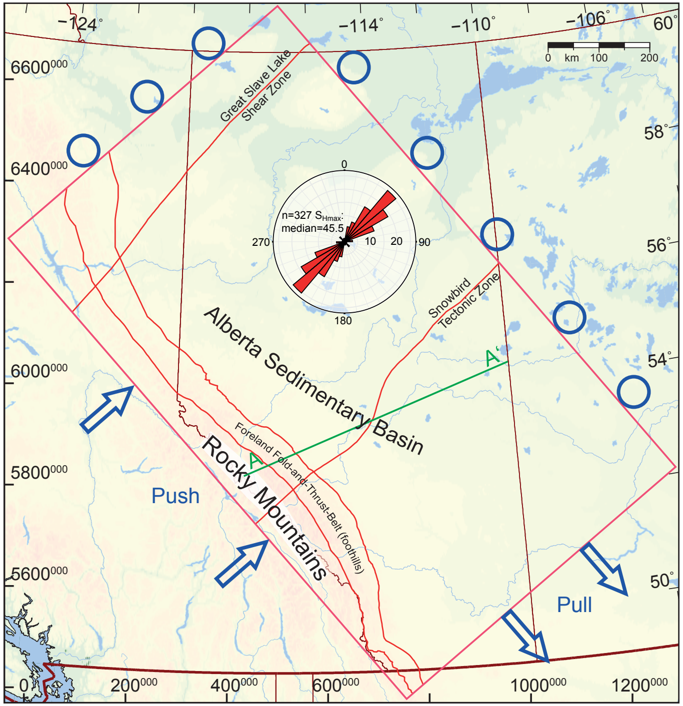

Figure 4. Map of Alberta with the model extent (red box), combined with the model features. Implemented are the main structural features (red lines), which are the front of the Rocky Mountains and the foothills, respectively, as well as the Snowbird Tectonic Zone and the Great Slave Lake Shear Zone. For comparison see tectonic map (Fig. 2). Push and pull along model sides and the allowed lateral motion are indicated by blue arrows and circles, respectively. The mean orientation of S_{Hmax} is indicated by a rose diagram; note that stress orientation is parallel and orthogonal, respectively, to the model box. The trace of the cross section in Fig. 3 is indicated by the green line.

SED
6, 2423–2494, 2014

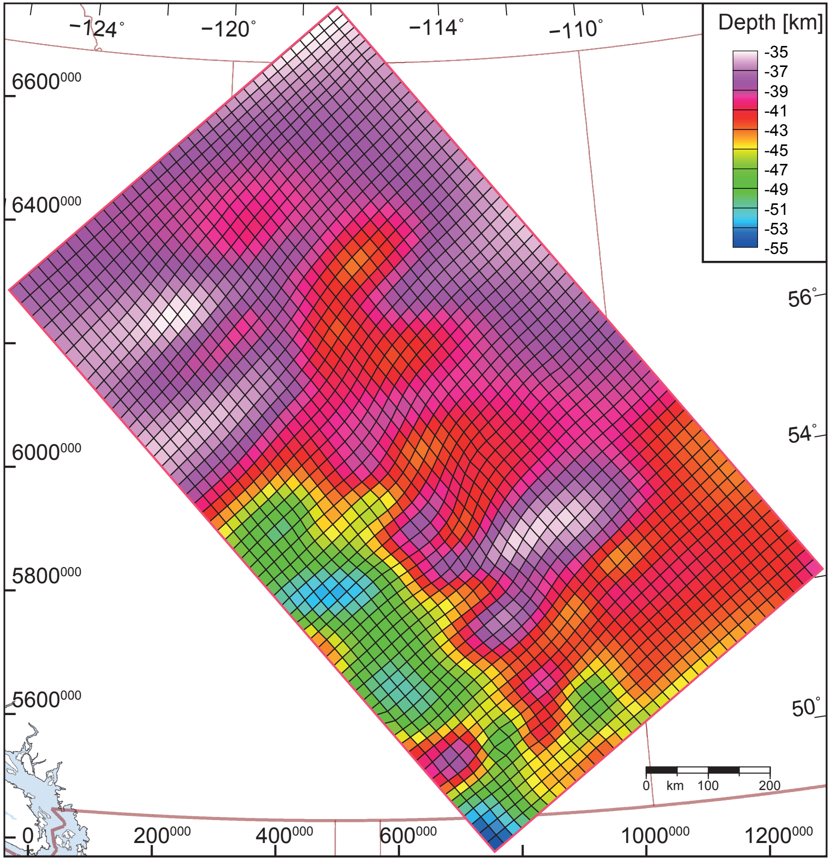

Figure 5. Topography of the Mohorovičić-discontinuity (Moho) within the model box. The map extend is indicated by geographical coordinates (top and right) and with UTM coordinates from Zone 11 (left and bottom). The mesh-size in that depth (∼ 20 km) is indicated by black lines.

SED
6, 2423–2494, 2014

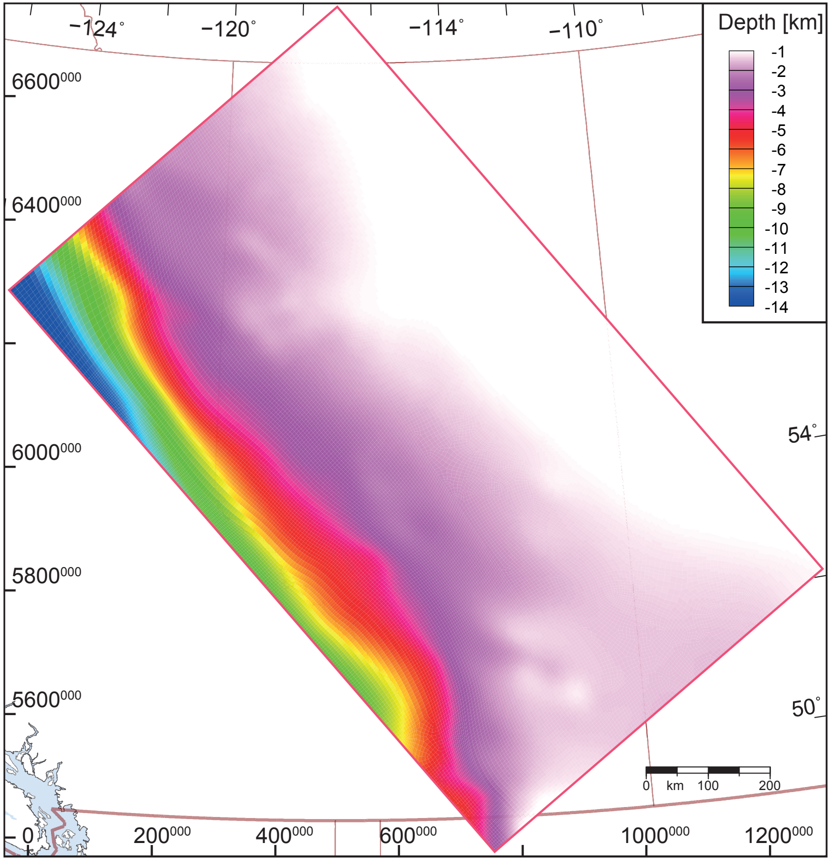

Figure 6. Topography of the basement top is shown within the model box. The map extent is indicated by geographical coordinates (top and right) and by UTM coordinates from Zone 11 (left and bottom).

SED
6, 2423–2494, 2014

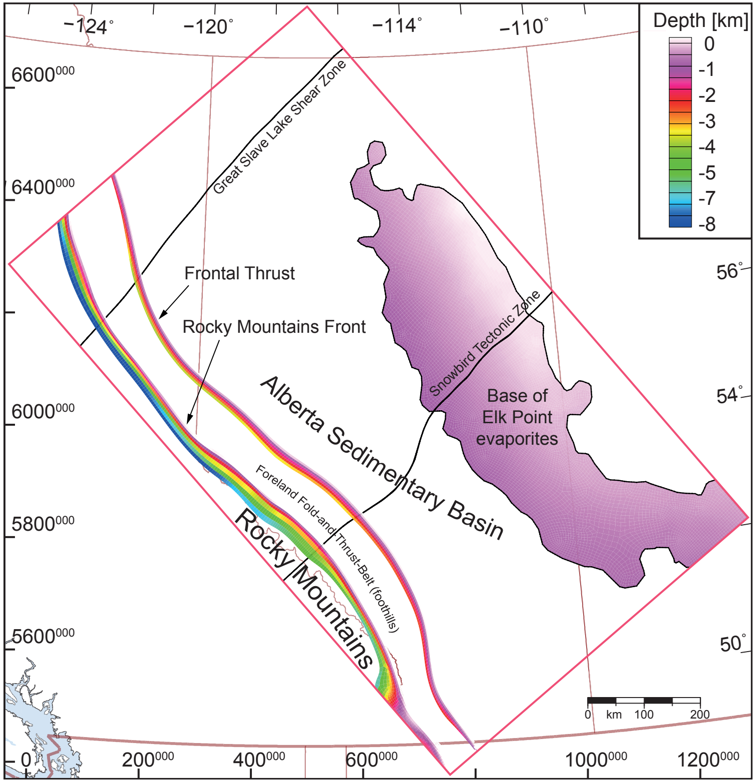

Figure 7. Upper crustal structures, used in the model. The units above the basement are separated in the basin, the foothills and the Rocky Mountains. The basin also contains a thin rock salt layer from the Elk Point group. Within the basement, the Great Slave Lake Shear Zone and the Snowbird Tectonic Zone are incorporated. The map extent is indicated by geographical coordinates (top and right) and by UTM coordinates from Zone 11 (left and bottom).

SED
6, 2423–2494, 2014

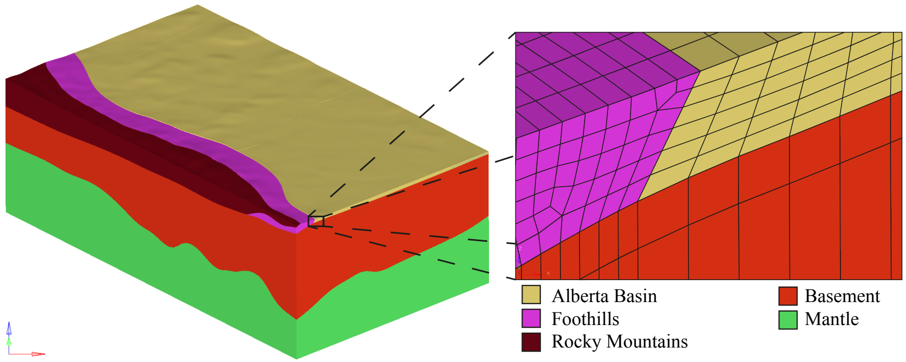

Figure 8. 3-D-view of the Alberta Model, view from south to north – rock units are indicated by colours. A small cut-out is zoomed in to see the mesh in detail. The vertical exaggeration is 5 times.

SED
6, 2423–2494, 2014

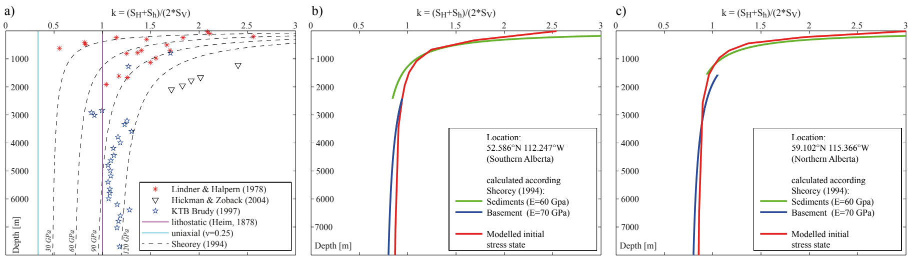

Figure 9. (a) Compilation of *k* ratios from North America (Lindner and Halpern, 1978), the SAFOD pilot hole (Hickman and Zoback, 2004) and from the KTB (Brudy et al., 1997). Theoretical *k* ratios based on the assumption of lithostatic load in greater depth (Heim, 1878, $k = 1$), uniaxial strain conditions (Eq. 2) and the distribution according to Sheorey (1994, Eq. 5) for Young's modulus $E = 30$, 60, 90 and 120 GPa are plotted. **(b)** and **(c)** Depth profile of the initial and calculated *k* values for two test sites within the model. Blue and green line indicates calculated *k* profiles based on Sheorey (1994, Eq. 5) and the associated Young's modulus. The red line indicates the *k* profiles from the model with the initial stress state.

SED
6, 2423–2494, 2014

K. Reiter and O. Heidbach

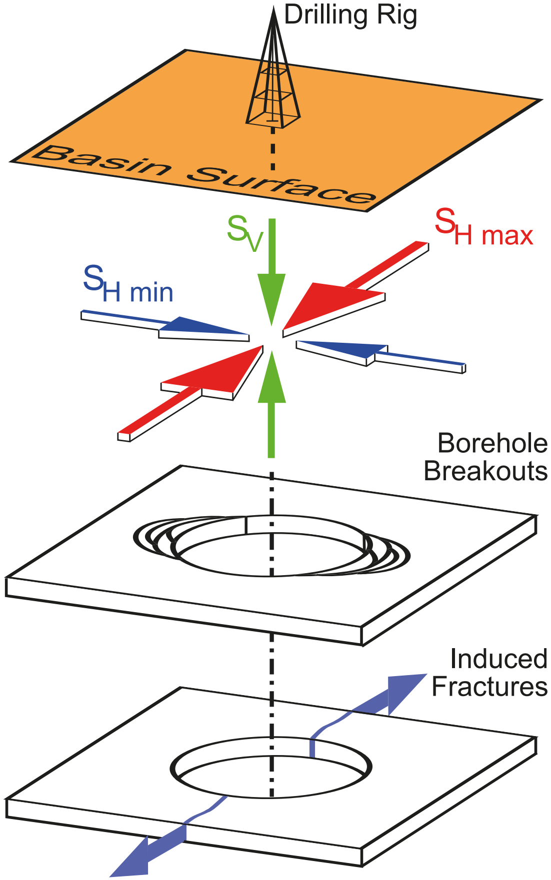

Figure 10. General assumption of stresses in sedimentary basins: The vertical stress (S_V) is a principal stress, thus perpendicular to the minimum and maximum horizontal stress (S_{hmin} and S_{Hmax}). Borehole breakouts occur in orientation of the S_{hmin} and induced tensile fractures occur in orientation of S_{Hmax}.

SED
6, 2423–2494, 2014

Calibration of 3-D crustal stress model Alberta Basin

K. Reiter and
O. Heidbach

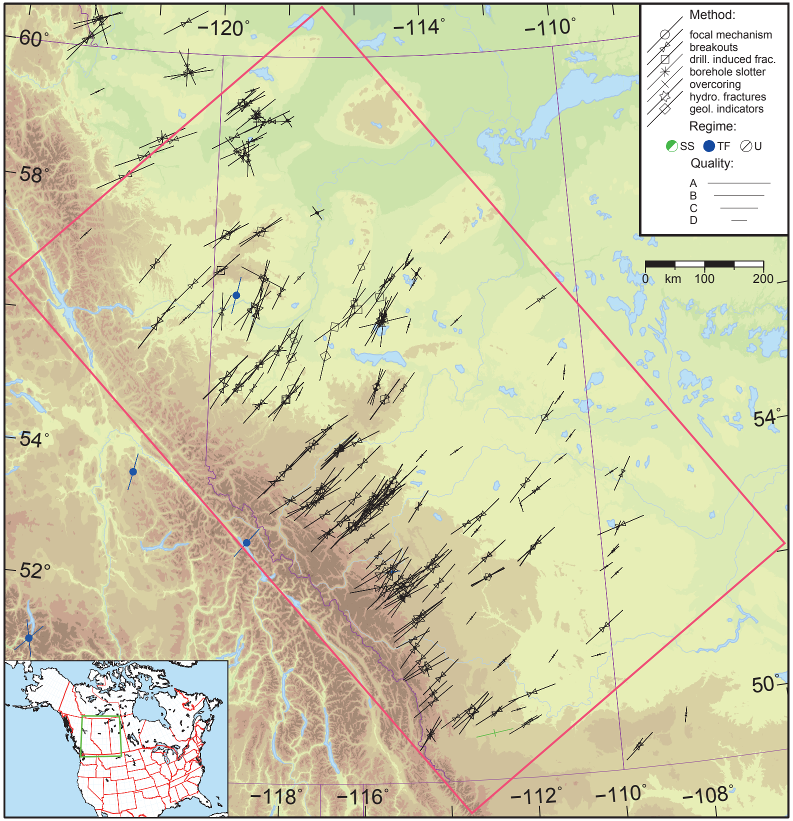

Figure 11. Crustal stress map of Alberta, lines represent orientations of maximum horizontal compressional stress S_{Hmax}, line length is proportional to the data quality. Colours indicate stress regimes, with green for strike-slip faulting (SS), blue for thrust faulting (TF), and black for unknown regime (U). In sum there are 321 S_{Hmax} azimuth data are available within the modelled region. Data are from the latest update of the Canadian Stress map (Reiter et al., 2014).

SED
6, 2423–2494, 2014

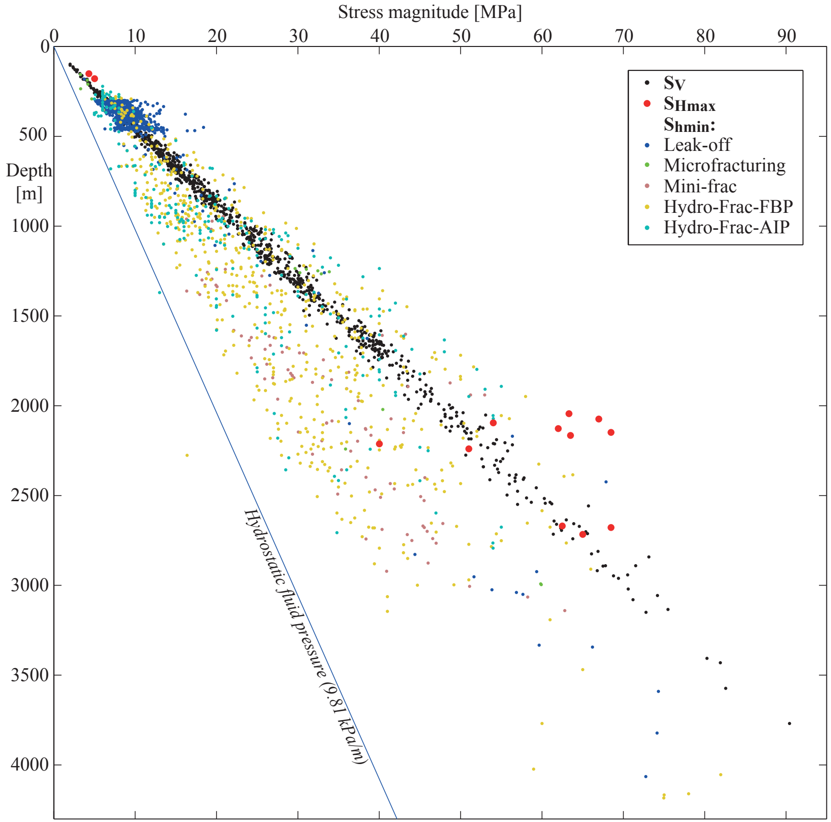

Figure 12. Depth plot of the in-situ stress magnitudes. These are 981 S_V magnitude data (black), 1720 S_{hmin} magnitudes (several colours) and 2 measured as well as 11 calculated S_{Hmax} magnitudes (highlighted red points). S_{hmin} data are colour coded depending on the test type, which is taken over from the original database.

SED
6, 2423–2494, 2014

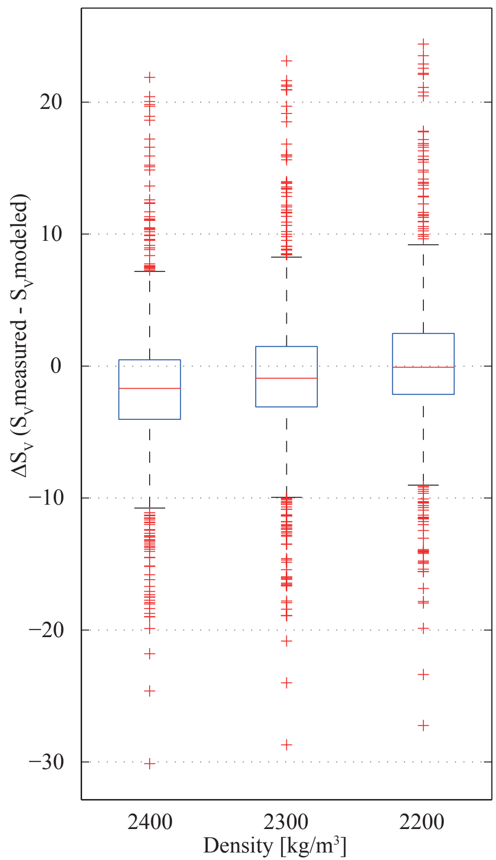

Figure 13. Boxplot of the varied density of the basin sediments – plotted is the ΔS_V. The median ΔS_V of the model with a density of 2200 kg m^{-3} is close to 0 MPa and therefore the *best-fit* density to the available S_V data, in contrast to the models with a higher basin density, where ΔS_V is negative (see Eq. 11).

SED
6, 2423–2494, 2014

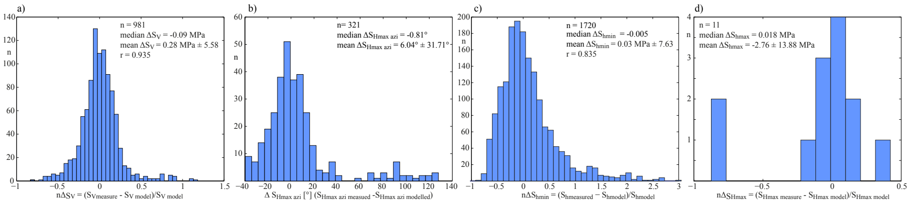

Figure 14. Distribution plots of the *best-fit* model, the number of data, the median, the mean, the standard deviation (SD) and the Pearson product-moment correlation coefficient (r) for the most $n\Delta S$ or ΔS are indicated in the histograms. **(a)** Histogram of the normalized ΔS_V displays a nice Gaussian distribution. **(b)** The histogram of the ΔS_Hmax azimuth data displays one major cluster around zero, with a range from −40 to 40°; a second smaller cluster ranges orientations between 70 to 130°, with the highest peak by about 90°. **(c)** The normalized ΔS_hmin magnitudes displays a positive screwed distribution; **(d)** the normalized ΔS_Hmax magnitude histogram for the 13 available data displays two negative outliers (the two shallow (overcoring) data). However the 11 calculated data are arranged around zero.

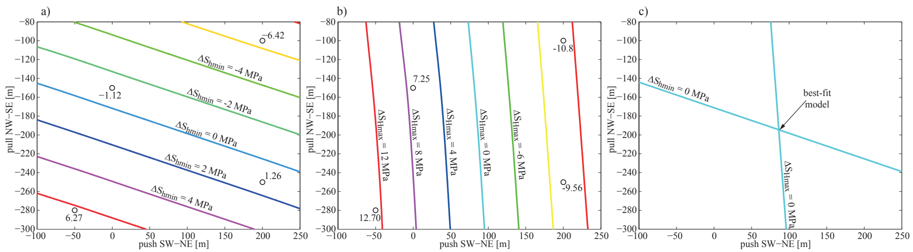

Figure 15. Plot of four models with different shortening or extension at the model boundary, see Table 2 for details. (**a** and **b**): the median S_{hmin} and the median S_{Hmax} are plotted depending on the north-west to south-east extension (pull) and the south-west to north-east shortening (push) The isolines of the median ΔS_{hmin} and ΔS_{Hmax} are colour coded. **(c)** The isolines, where the median ΔS_{hmin} and ΔS_{Hmax} is zero are plotted alone. The intersection of both isolines indicated the push-pull values where the *best-fit* model can be found.

SED
6, 2423–2494, 2014

Calibration of 3-D crustal stress model Alberta Basin

K. Reiter and O. Heidbach

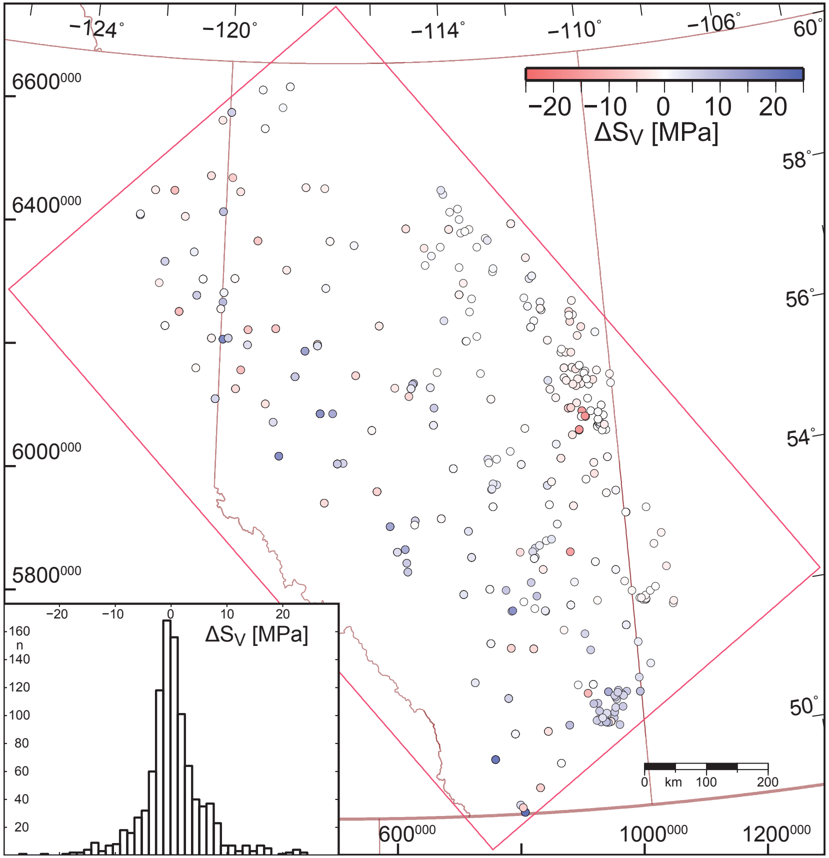

Figure 16. Spatial distribution of ΔS_V differences are plotted colour coded. The map extent is indicated by geographical coordinates (top and right) and by UTM coordinates from Zone 11 (left and bottom).

SED
6, 2423–2494, 2014

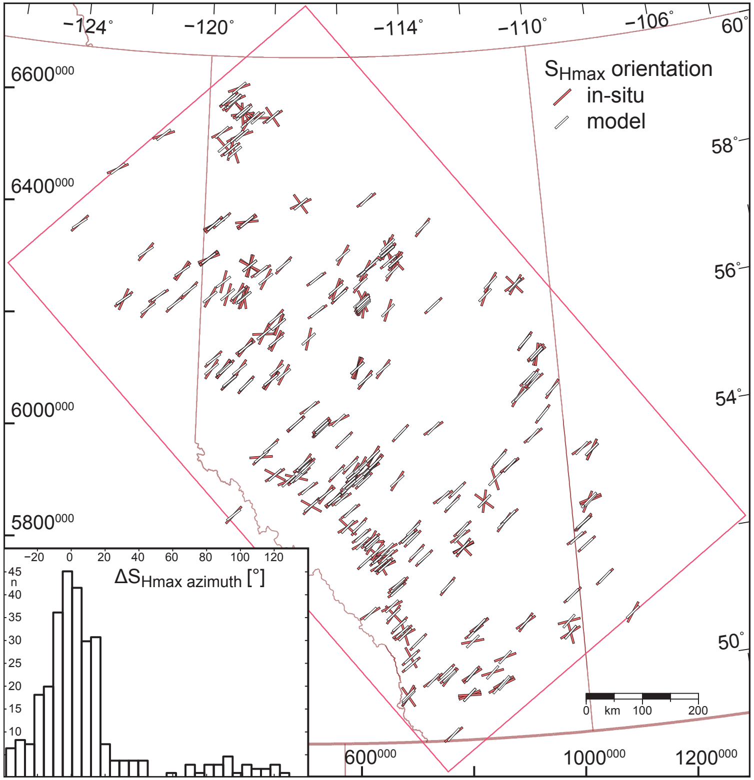

Figure 17. Spatial distribution of the modelled and the in-situ S_{Hmax} azimuth data. A good fit of modelled data is reached, except some suggested misinterpreted data (±90°) and a systematic rotations, close to the Peace River Arch (56° N, 118° W) and close to the Bow Island Arch (50° N, 114° W). The map extent is indicated by geographical coordinates (top and right) and by UTM coordinates from Zone 11 (left and bottom).

SED
6, 2423–2494, 2014

Calibration of 3-D crustal stress model Alberta Basin

K. Reiter and
O. Heidbach

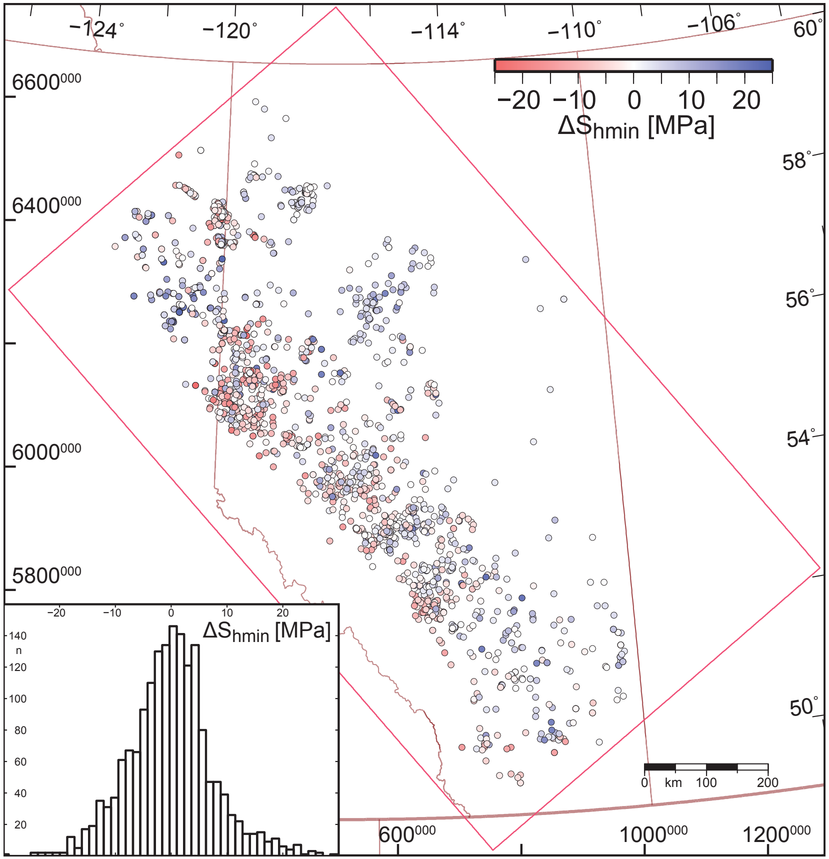

Figure 18. Comparison of the modelled and the in-situ S_{hmin} magnitudes, plotted as ΔS_{hmin}. The map extent is indicated by geographical coordinates (top and right) and by UTM coordinates from Zone 11 (left and bottom).

SED
6, 2423–2494, 2014

Calibration of 3-D crustal stress model Alberta Basin

K. Reiter and O. Heidbach

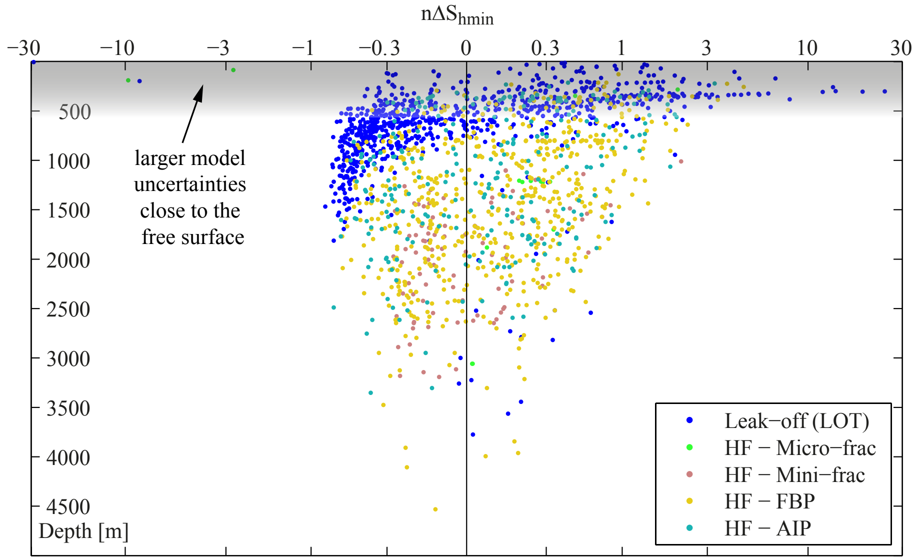

Figure 19. The distribution of the normalized ΔS_{hmin} vs. depth, the measurement method is colour coded. Results close to the surface up to about −500 m (indicated by greyish haze) have to be interpreted with care, as interpolation of the integration points to the nodes of the finite elements at the surface is problematic. Note that shallow (< −500 m) leak-off tests (LOT) deliver systematic higher magnitudes than the stress model. In contrast to that are deeper (> −500 m) LOT data, which have systematically smaller magnitudes as the model. Hydraulic fracturing (HF) data are unconcerned from such systematic drift.

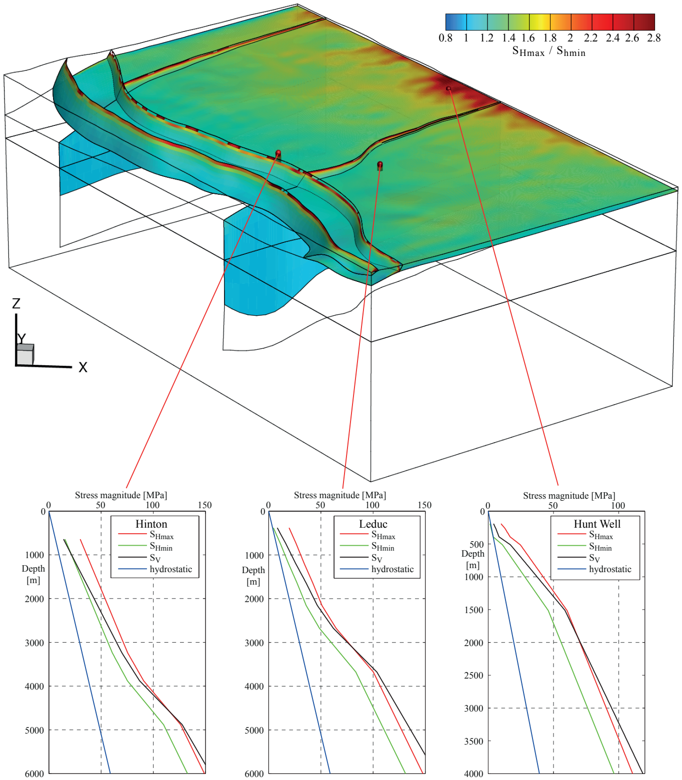

Figure 20. 3-D view of the *best-fit* model. Displayed is the $S_{\text{Hmax}}/S_{\text{hmin}}$ ratio, plotted at the basement top, along the Snowbird- and the Great Slave Tectonic Shear Zone, the Rocky Mountains front and the front of the foothills. Three virtual wells from the surface down into the basement are indicated in the model. The stress growth into depth is illustrated in the lower part. These are virtual wells in Hinton, in Leduc (30 km south of Edmonton) and the location of the Hunt well (15 km west of Fort McMurray). The shallowest part is not shown in the plots due to free surface effects.